

Femtoscopic analysis of pp collisions at $\sqrt{s} = 0.9$ and 7 TeV at the LHC with two-pion Bose-Einstein correlations

K. Aamodt *et al.**

(ALICE Collaboration)

(Received 20 January 2011; published 14 December 2011)

We report on the high statistics two-pion correlation functions from pp collisions at $\sqrt{s} = 0.9$ TeV and $\sqrt{s} = 7$ TeV, measured by the ALICE experiment at the Large Hadron Collider. The correlation functions as well as the extracted source radii scale with event multiplicity and pair momentum. When analyzed in the same multiplicity and pair transverse momentum range, the correlation is similar at the two collision energies. A three-dimensional femtoscopic analysis shows an increase of the emission zone with increasing event multiplicity as well as decreasing homogeneity lengths with increasing transverse momentum. The latter trend gets more pronounced as multiplicity increases. This suggests the development of space-momentum correlations, at least for collisions producing a high multiplicity of particles. We consider these trends in the context of previous femtoscopic studies in high-energy hadron and heavy-ion collisions and discuss possible underlying physics mechanisms. Detailed analysis of the correlation reveals an exponential shape in the outward and longitudinal directions, while the sideward remains a Gaussian. This is interpreted as a result of a significant contribution of strongly decaying resonances to the emission region shape. Significant nonfemtoscopic correlations are observed, and are argued to be the consequence of “mini-jet”-like structures extending to low p_T . They are well reproduced by the Monte-Carlo generators and seen also in $\pi^+\pi^-$ correlations.

DOI: [10.1103/PhysRevD.84.112004](https://doi.org/10.1103/PhysRevD.84.112004)

PACS numbers: 25.75.-q, 25.75.Gz, 25.70.Pq

I. INTRODUCTION

Proton-proton collisions at $\sqrt{s} = 0.9$ TeV and $\sqrt{s} = 7$ TeV have been recorded by A Large Ion Collider Experiment (ALICE) at the Large Hadron Collider (LHC) at CERN in 2010. These collisions provide a unique opportunity to probe Quantum Chromodynamics (QCD) in the new energy regime. The distinguishing feature of QCD is the mechanism of color confinement, the physics of which is not fully understood, due, in part, to its theoretical intractability [1]. The confinement mechanism has a physical scale of the order of the proton radius and is especially important at low momentum. The study presented in this work aims to measure the space-time extent of the source on this scale.

Two-pion correlations at low relative momentum were first shown to be sensitive to the interaction volume of the emitting source in $\bar{p} + p$ collisions by G. Goldhaber, S. Goldhaber, W. Lee, and A. Pais 50 years ago [2]. Since then, they were studied in $e^+ + e^-$ [3], hadron- and lepton-hadron [4], and heavy-ion [5] collisions. Especially in the latter case, two-particle femtoscopy has been developed into a precision tool to probe the dynamically-generated geometry structure of the emitting system. In particular, a

sharp phase transition between the color-deconfined and confined states was precluded by the observation of short time scales, and femtoscopic measurement of bulk collective flow proved that a strongly self-interacting system was created in the collision [6,7].

Femtoscopic analysis in heavy-ion collisions is believed to be understood in some detail, see e.g. [5]. The spatial scales grow naturally with the multiplicity of the event. Strong hydrodynamical collective flow in the longitudinal and transverse directions is revealed by dynamical dependencies of femtoscopic scales. The main puzzling aspect of the data is the relative energy independence of the results of the measurements.

To some extent, Bose-Einstein correlations in particle physics were initially of interest only as a source of systematic uncertainty in the determination of the W boson mass [8]. But overviews [3,4,9] of femtoscopic measurements in hadron- and lepton-induced collisions reveal systematics surprisingly similar to those mentioned above for heavy-ion collisions. Moreover, in the first direct comparison of femtoscopy in heavy-ion collisions at Relativistic Heavy-Ion Collider (RHIC) and proton collisions in the same apparatus an essentially identical multiplicity- and momentum dependence was reported in the two systems [10]. However, the multiplicities at which the femtoscopic measurement in pp collisions at RHIC was made were still significantly smaller than those in even the most peripheral heavy-ion collisions. In this work we are, for the first time, able to compare femtoscopic radii measured in pp and heavy-ion collisions at comparable event multiplicities. At

*Full author list given at the end of the article.

these multiplicities the observed correlations may be influenced by jets [11] while other studies suggest that a system behaving collectively may be created [12,13].

In our previous work [14] we reported that a multiplicity integrated measurement does not show any pair momentum dependence of the R_{inv} radius measured in the Pair Rest Frame (PRF). Similar analysis from the CMS Collaboration [15] also mentions that no momentum dependence was observed. However the analysis in two multiplicity ranges suggested that momentum dependence may change with multiplicity, although any strong conclusions were precluded by limited statistics. In this work we explored this dependence by using high statistics data and more multiplicity ranges. It enabled us to perform the three-dimensional analysis in the Longitudinally Co-Moving System (LCMS), where the pair momentum along the beam vanishes.

The paper is organized as follows: in Sec. II we describe the ALICE experimental setup and data taking conditions for the sample used in this work. In Sec. III we present the correlation measurement and characterize the correlation functions themselves. In Sec. IVA we show the main results of this work: the three-dimensional radii extracted from the data. We discuss various observed features and compare the results to other experiments. In Sec. V we show, for completeness, the one-dimensional R_{inv} analysis. Finally in Sec. VI we summarize our results. All the numerical values can be obtained from the Durham Reaction Database [16].

II. ALICE DATA TAKING

In this study we report on the analysis of pp collisions recorded by the ALICE experiment during the 2010 run of the LHC. Approximately 8×10^6 events, triggered by a minimum-bias trigger at the injection energy of $\sqrt{s} = 0.9$ TeV, and 100×10^6 events with similar trigger at the maximum LHC energy to date, $\sqrt{s} = 7$ TeV, were analyzed in this work.

The ALICE Time Projection Chamber (TPC) [17] was used to record charged-particle tracks as they left ionization trails in the Ne – CO₂ gas. The ionization drifts up to 2.5 m from the central electrode to the end caps to be measured on 159 padrows, which are grouped into 18 sectors; the position at which the track crossed the padrow was determined with resolutions of 2 mm and 3 mm in the drift and transverse directions, respectively. The momentum resolution is $\sim 1\%$ for pions with $p_t = 0.5$ GeV/ c . The ALICE Inner Tracking System (ITS) was also used for tracking. It consists of six silicon layers, two innermost Silicon Pixel Detector (SPD) layers, two Silicon Drift Detector (SDD) layers, and two outer Silicon Strip Detector (SSD) layers, which provide up to six space points for each track. The tracks used in this analysis were reconstructed using the information from both the TPC and the ITS; such tracks were also used to reconstruct

the primary vertex of the collision. For details of this procedure and its efficiency see [18]. The forward scintillator detectors VZERO are placed along the beam line at +3 m and -0.9 m from the nominal interaction point. They cover a region $2.8 < \eta < 5.1$ and $-3.7 < \eta < -1.7$, respectively. They were used in the minimum-bias trigger and their timing signal was used to reject the beam-gas and beam-halo collisions.

The minimum-bias trigger required a signal in either of the two VZERO counters or one of the two inner layers of the Silicon Pixel Detector (SPD). Within this sample, we selected events based on the measured charged-particle multiplicity within the pseudorapidity range $|\eta| < 1.2$. Events were required to have a primary vertex within 1 mm of the beam line and 10 cm of the center of the 5 m long TPC. This provides almost uniform acceptance for particles with $|\eta| < 1$ for all events in the sample. It decreases for $1.0 < |\eta| < 1.2$. In addition, we require events to have at least one charged particle reconstructed within $|\eta| < 1.2$.

The minimum number of clusters associated to the track in the TPC is 70 (out of the maximum of 159) and 2 in the ITS (out of the maximum of 6). The quality of the track is determined by the χ^2/N value for the Kalman fit to the reconstructed position of the TPC clusters (N is the number of clusters attached to the track); the track is rejected if the value is larger than 4.0 (2 degrees of freedom per cluster). Tracks with $|\eta| < 1.2$ are taken for the analysis. The p_t of accepted particles has a lower limit of 0.13 GeV/ c because tracks with lower p_t do not cross enough padrows in the TPC. The efficiency of particle reconstruction is about 50% at this lowest limit and then quickly increases and reaches a stable value of approximately 80% for $p_t > 0.2$ GeV/ c . In order to reduce the number of secondary particles in our sample, we require the track to project back to the primary interaction vertex within $0.018 + 0.035p_t^{-1.01}$ cm in the transverse plane and 0.3 cm in the longitudinal direction (so-called Distance of Closest Approach or DCA selection).

ALICE provides an excellent particle identification capability through the combination of the measurement of the specific ionization (dE/dx) in the TPC and the ITS and the timing signals in the ALICE Time Of Flight (TOF). In the momentum range covered here (0.13 GeV/ c to 0.7 GeV/ c) pions constitute the majority of particles. We use only the TPC measurement for Particle Identification (PID) in this work, as the other detectors offer significant improvement at higher p_t than used here. This PID procedure results in a small contamination of the pion sample by electrons at $p_t < 0.2$ GeV/ c and kaons at $p_t > 0.65$ GeV/ c . Allowing other particles into our sample has only a minor effect of lowering the strength of the correlation (the λ parameter), while it does not affect the femtoscopic radius, so we do not correct for it explicitly. The amount of electron contamination is less than 5%; kaons

contaminate the pion sample for $p > 0.6$ GeV/ c ; their fraction is less than 10%.

III. CORRELATION FUNCTION MEASUREMENT

Experimentally, the two-particle correlation function is defined as the ratio $C(\mathbf{q}) = A(\mathbf{q})/B(\mathbf{q})$, where $A(\mathbf{q})$ is the measured two-pion distribution of pair momentum difference $\mathbf{q} = \mathbf{p}_2 - \mathbf{p}_1$, and $B(\mathbf{q})$ is a similar distribution formed by using pairs of particles from different events [19].

The size of the data sample used for this analysis allowed for a highly differential measurement. In order to address the physics topics mentioned in the introduction, the analysis was performed simultaneously as a function of the total event multiplicity N_{ch} and pair transverse momentum $k_T = |\vec{p}_{t,1} + \vec{p}_{t,2}|/2$. For the multiplicity determination we counted the tracks reconstructed simultaneously in the ITS and the TPC, plus the tracks reconstructed only in the ITS in case the track was outside of the TPC η acceptance. The total number of events accepted after applying the selection criteria in the $\sqrt{s} = 7$ TeV sample was 60×10^6 and in the $\sqrt{s} = 0.9$ TeV sample it was 4.42×10^6 . We divided the full multiplicity range into eight and four ranges for the two energies, respectively, in such a way that the like-charge pion pair multiplicity in each of them was comparable. Table I gives (a) values for the range of raw charged-particle multiplicity that was used to categorize the event, (b) the corresponding mean charge particle density $\langle dN_{\text{ch}}/d\eta \rangle$ as well as (c) number of events and (d) the number of identical pion pairs in each range. The femtoscopic measurement requires the events to have at least one charged pion identified¹ and its momentum determined. We give the $dN_{\text{ch}}/d\eta$ values in Table I for this event sample. We denote this value as $\langle dN_{\text{ch}}/d\eta \rangle|_{N_{\text{ch}} \geq 1}$; its typical uncertainty is 10%. We note that for the lowest multiplicity this charged-particle density is biased towards higher values with respect to the full sample of inelastic events.

The pair momentum k_T ranges used in the analysis were (0.13, 0.2), (0.2, 0.3), (0.3, 0.4), (0.4, 0.5), (0.5, 0.6), (0.6, 0.7) GeV/ c .

A. Correlation function representations

The correlations are measured as a function of pair relative momentum four-vector \mathbf{q} . We deal with pions, so the masses of the particles are fixed—in this case \mathbf{q} reduces to a vector: \vec{q} . The one-dimensional analysis is performed versus the magnitude of the invariant momentum difference $q_{\text{inv}} = |\vec{q}|$, in the PRF. The large available statistics for this work allowed us to perform a detailed analysis also for the three-dimensional functions. In forming them, we calculate the momentum difference in the LCMS and

¹In fact the correlation signal is constructed from events having at least *two* same-charge pions (a pair). The one-pion events do contribute to the mixed background.

TABLE I. Multiplicity selection for the analyzed sample. Uncorrected N_{ch} in $|\eta| < 1.2$, $\langle dN_{\text{ch}}/d\eta \rangle|_{N_{\text{ch}} \geq 1}$ (see text for the definition), number of events, and number of identical pion pairs in each range are given.

Bin	N_{ch}	$\langle dN_{\text{ch}}/d\eta \rangle _{N_{\text{ch}} \geq 1}$	No. events $\times 10^6$	No. pairs $\times 10^6$
$\sqrt{s} = 0.9$ TeV				
1	1–11	2.5	3.1	8.8
2	12–16	6.4	0.685	8.6
3	17–22	9.0	0.388	9.5
4	23–80	13.0	0.237	12.9
$\sqrt{s} = 7$ TeV				
1	1–11	2.8	31.4	48.7
2	12–16	6.6	9.2	65.0
3	17–22	9.2	7.4	105.7
4	23–28	12.0	4.8	120.5
5	29–34	14.9	3.0	116.3
6	35–41	17.9	2.0	115.6
7	42–51	21.4	1.3	114.5
8	52–151	27.6	0.72	108.8

decompose this \vec{q}_{LCMS} according to the Bertsch-Pratt [20,21] “out-side-long” (sometimes indicated by o , s , and l subscripts) parametrization. Here, q_{long} is parallel to the beam, q_{out} is parallel to the pair transverse momentum, and q_{side} is perpendicular to q_{long} and q_{out} . If one wishes to compare the radii measured in the LCMS to R_{inv} one needs to multiply one of the transverse radii in the LCMS (the one along the pair transverse momentum) by the Lorentz γ corresponding to the pair transverse velocity and then average the three radii. Therefore an R_{inv} constant with momentum is consistent with the radii in the LCMS decreasing with momentum. Figure 1 shows one-dimensional projections of the three-dimensional correlation function $C(q_{\text{out}}, q_{\text{side}}, q_{\text{long}})$ onto the q_{out} , q_{side} , and q_{long} axes, for π^+ pairs from one of the multiplicity/ k_T ranges from the $\sqrt{s} = 7$ TeV sample. The function is normalized with a factor that is a result of the fit (the details of the procedure are described in Sec. III D); unity means no correlation.

The one-dimensional projections, shown in Fig. 1, present a limited view of the three-dimensional structure of the correlation function. It is increasingly common to represent correlation functions in a harmonic analysis [22–24]; this provides a more complete representation of the three-dimensional structure of the correlation, a better diagnostic of nonfemtoscopic correlations [23], and a more direct relation to the shape of the source [25]. The moments of the Spherical Harmonic (SH) decomposition are given by

$$A_l^m(|\vec{q}|) \equiv \frac{1}{\sqrt{4\pi}} \int d\phi d(\cos\theta) C(|\vec{q}|, \theta, \phi) Y_l^m(\theta, \phi). \quad (1)$$

Here, the out-side-long space is mapped onto Euler angles in which $q_{\text{long}} = |\vec{q}| \cos\theta$ and $q_{\text{out}} = |\vec{q}| \sin\theta \cos\phi$. For

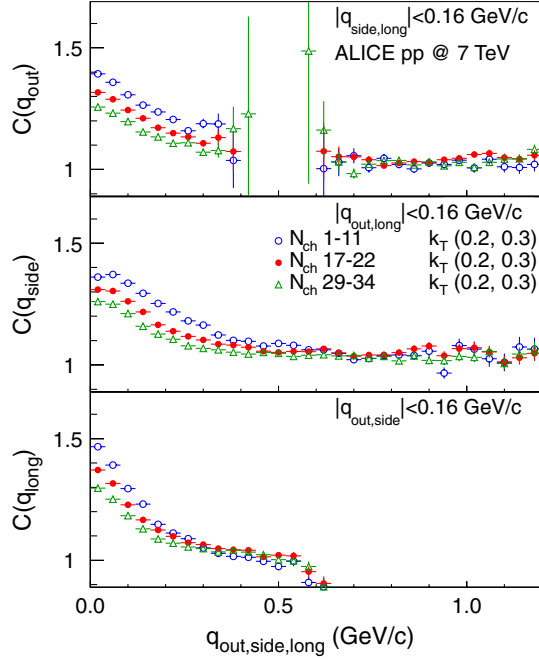


FIG. 1 (color online). Projections of the three-dimensional Cartesian representations of the correlation functions onto the q_{out} , q_{side} , and q_{long} axes for pairs with $0.2 < k_T < 0.3$ GeV/ c , for three multiplicity ranges. To project onto one q component, the others are integrated over the range 0–0.16 GeV/ c .

pairs of identical particles in collider experiments done with symmetrical beams, including the analysis in this work, the odd l and the imaginary and odd m components for even l vanish. The first three nonvanishing moments, which capture essentially all of the three-dimensional structure, are then C_0^0 , C_2^0 , and C_2^2 . These are shown in Fig. 2. The components for $l \geq 4$ represent the fine details of the correlation structure and are not analyzed in this work.

The C_0^0 is the angle-averaged component. It captures the general shape of the correlation. The width of the peak near $q = 0$ is inversely proportional to the overall femtoscopic size of the system. The C_2^0 component is the correlation weighed with the $\cos^2(\theta)$. If it differs from 0, it signifies that the longitudinal and transverse sizes of the emission region differ. The C_2^2 is weighed with $\cos^2(\phi)$. If it differs from 0, it signals that the outward and sideward sizes differ. The correlation function is normalized to the number of pairs in the background divided by the number of pairs in the signal.

B. Measured correlations

In Figs. 1 and 2 we show selected correlations to illustrate how they depend on multiplicity. This is done for k_T of (0.2, 0.3) GeV/ c ; the behavior in other k_T ranges and at the lower collision energy is qualitatively the same. The narrowing of the correlation peak with increasing multiplicity is apparent, corresponding to the increase of the size

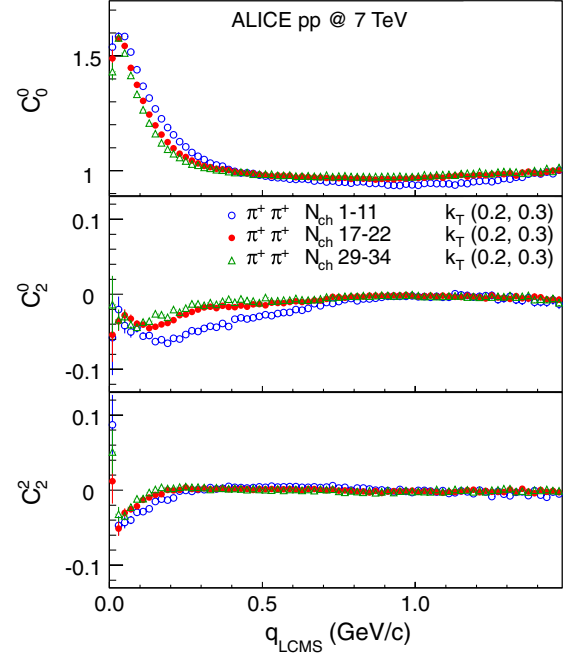


FIG. 2 (color online). Moments of the SH decomposition of the correlation functions for pairs with $0.2 < k_T < 0.3$ GeV/ c , for three multiplicity ranges.

of the emitting region. The behavior of the correlation function at large q is also changing, the low multiplicity baseline is not flat, goes below 1.0 around $q = 1$ GeV/ c , and then rises again at larger q ; for higher multiplicities the background becomes flatter at large q . In the Cartesian representation shown in Fig. 1, areas with no data points (acceptance holes) are seen in q_{out} projection near $q = 0.5$ GeV/ c and in q_{long} above 0.6 GeV/ c . Since q_{long} is proportional to the difference of longitudinal momenta, its value is limited due to η acceptance. In the *out* direction the hole appears due to a combination of lower p_t cut off and the selected k_T range. It can be simply understood as follows: For the projection in the upper panel of Fig. 1, we take the value of q_{side} and q_{long} small. The value of q_{side} is proportional to the azimuthal angle difference, while q_{long} is proportional to polar angle difference. For $q_{side}, q_{long} = 0$, q_{out} is simply $p_{t,2} - p_{t,1}$ and k_T is $(p_{t,1} + p_{t,2})/2$, where p_t is no longer a two-vector but just a scalar. The particles are either fully aligned (both p_t 's are positive or both are negative) or back-to-back (one p_t is positive, the other negative). When we combine the lower p_t cut off $|p_t| > 0.13$ GeV/ c and the k_T selection $0.2 \leq k_T \leq 0.3$, it can be shown that some range of the q_{out} values is excluded. This range will depend on the k_T selection.

The k_T dependence of the correlation function is shown in Figs. 3 and 4, for multiplicity $17 \leq N_{ch} \leq 22$. The behavior in other multiplicity ranges and at lower energy is qualitatively similar (except the lowest multiplicity bin where the behavior is more complicated—see the discussion of the extracted radii in Sec. III D for details). We see a

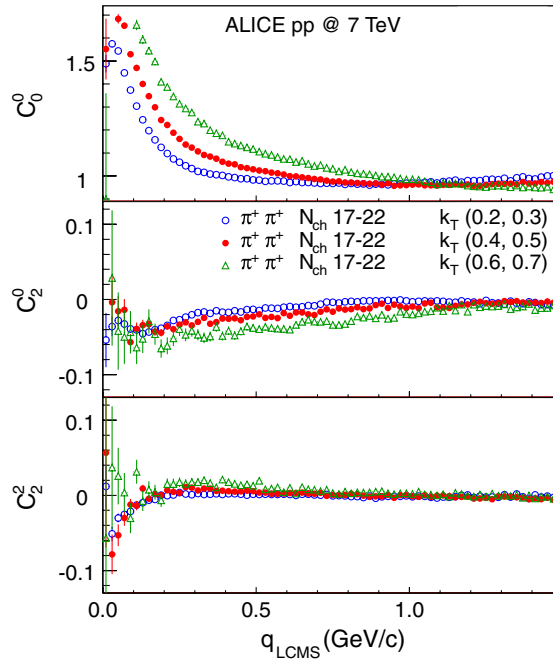


FIG. 3 (color online). Moments of the SH decomposition of the correlation functions for events with $17 \leq N_{\text{ch}} \leq 22$, for three k_T ranges.

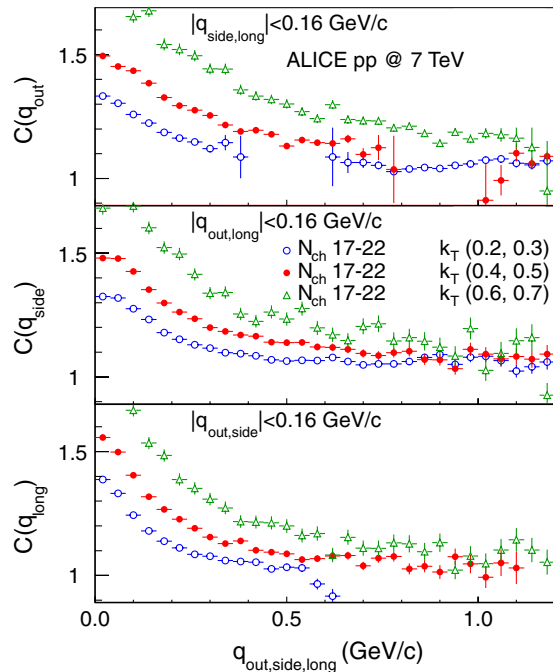


FIG. 4 (color online). Projections of the three-dimensional Cartesian representations of the correlation functions onto the q_{out} , q_{side} , and q_{long} axes, for events with $17 \leq N_{\text{ch}} \leq 22$, for three k_T ranges. To project onto one q component, the others are integrated over the range 0–0.16 GeV/c.

strong change of the correlation with k_T , with two apparent effects. At low k_T the correlation appears to be dominated by the femtoscopic effect at $q < 0.3$ GeV/c and is flat at larger q . As k_T grows, the femtoscopic peak broadens (corresponding to a decrease in size of the emitting region). In addition, a wide structure, extending up to 1.0 GeV/c in q for the highest k_T range, appears. We analyze this structure in further detail later in this work. We also see that, according to expectations, the acceptance holes in the out and long region move as we change the k_T range.

Figure 5 shows the example of the correlation function, for the same multiplicity/ k_T range, for pp collisions at two collision energies. We note a similarity between the two functions; the same is seen for other k_T 's and overlapping multiplicity ranges. The similarity is not trivial: changing the multiplicity by 50%, as seen in Fig. 2 or k_T by 30% as seen in Fig. 3 has a stronger influence on the correlation function than changing the collision energy by an order of magnitude. We conclude that the main scaling variables for the correlation function are global event multiplicity and transverse momentum of the pair; the dependence on collision energy is small. The energy independence of the emission region size is the first important physics result of this work. We emphasize that it can be already drawn from the analysis of the correlation functions themselves, but we will also perform more qualitative checks and discussions when we report the fitted emission region sizes in Sec. IV.

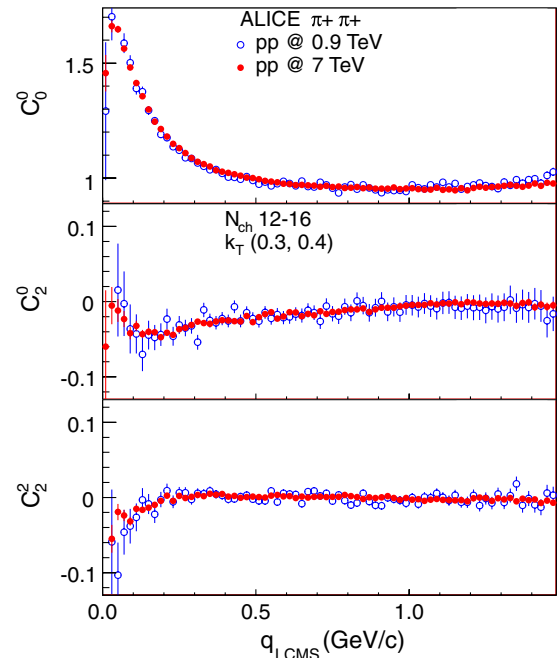


FIG. 5 (color online). Moments of the SH decomposition of the correlation functions for events with $12 \leq N_{\text{ch}} \leq 16$, pairs with $0.3 < k_T < 0.4$ GeV/c. Open symbols are for $\sqrt{s} = 0.9$ TeV collisions, closed symbols for $\sqrt{s} = 7$ TeV collisions.

C. Nonfemtoscopic correlation structures

In Fig. 3 we noted the appearance of long-range structures in the correlation functions for large k_T . If these were of femtoscopic origin, they would correspond to an unusually small emission region size of 0.2 fm. We reported the observation of these structures in our previous analysis [14] at $\sqrt{s} = 0.9$ TeV, where they were interpreted as nonfemtoscopic correlations coming from mini-jet-like structures at $p_t < 1$ GeV/c. Here we further analyze this hypothesis. In Fig. 6 we show the comparison of the correlation function at multiplicity $12 \leq N_{\text{ch}} \leq 16$ in an intermediate k_T range, where the long-range correlations are apparent, to the Monte-Carlo (MC) calculation. The simulation used the PYTHIA generator [26], Perugia-0 tune [27] as input. In this model the enhanced pair production at small relative angle (which is equivalent to small q in the k_T ranges considered here) is associated with soft parton fragmentation or mini-jets. The particles generated were propagated through the full simulation of the ALICE detector [17]. Then they were reconstructed and analyzed in exactly the same way as our real data, using the same multiplicity and k_T ranges. The MC calculation does not include the wave-function symmetrization for identical particles; hence, the absence of the femtoscopic peak at low q is expected. In the angle-averaged C_0^0 component a significant correlation structure is seen, up to 1 GeV/c, with a slope similar to the data outside of the peak at low q . Similarly, in the C_2^0 component a weak and wide correlation dip is seen around

$q = 0.5$ GeV/c, which is also seen in the data. In MC, the correlation in C_2^0 disappears at lower q , while for the data it extends to much lower q , exactly where the femtoscopic peak is expected and seen in C_0^0 . Our hypothesis is that both the long-range peak in C_0^0 and the dip in C_2^0 are of a mini-jet origin. They need to be taken into account when fitting the correlation function from data, so that the femtoscopic peak can be properly extracted and characterized. The calculations were also carried out with a second Monte-Carlo, the PHOJET model [28,29], and gave similar results. The differences between the two models are reflected in the systematic error.

In order to characterize the nonfemtoscopic background we study in detail the correlation structure in the MC generators, in exactly the same multiplicity/ k_T ranges as used for data analysis. We see trends that are consistent with the mini-jet hypothesis. The correlation is small or nonexistent for low p_t (first k_T range) and it grows strongly with p_t . In Fig. 7 we show this structure for selected multiplicity/ k_T at both energies. At the highest k_T the effect has the magnitude of 0.3 at low q , comparable to the height of the femtoscopic peak. The appearance of these correlations is the main limiting factor in the analysis of the k_T dependence. We tried to analyze the correlations at k_T higher than 0.7 GeV/c, but we were unable to obtain a meaningful femtoscopic result, because the mini-jet structure was dominating the correlation. The strength of the correlation decreases with growing multiplicity (as

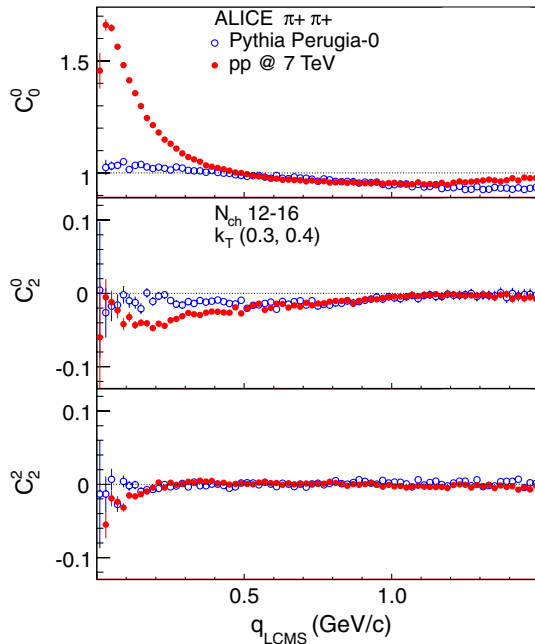


FIG. 6 (color online). Moments of the SH decomposition of the correlation functions for events with $12 \leq N_{\text{ch}} \leq 16$, pairs with $0.3 < k_T < 0.4$ GeV/c. Open symbols are PYTHIA MC simulations (Perugia-0 tune), closed symbols are ALICE data from $\sqrt{s} = 7$ TeV collisions.

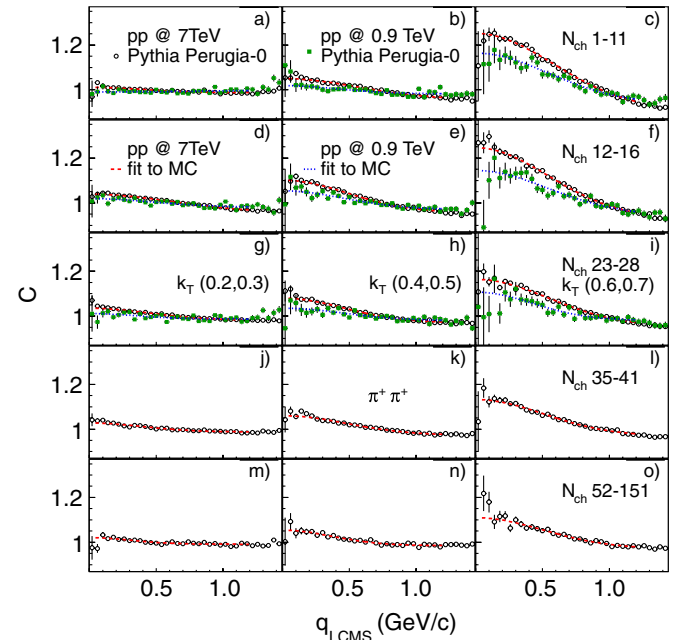


FIG. 7 (color online). Summary of the MC simulations for selected multiplicity and k_T intervals, open symbols are a simulation at $\sqrt{s} = 7$ TeV, closed symbols at $\sqrt{s} = 0.9$ TeV. Dashed lines are Gaussian fits to the simulations to determine the background parameters (see text for details).

expected), slower than $1/N_{\text{ch}}$, so that it is still significant at the highest multiplicity. We studied other tunes of the PYTHIA model and found that the Perugia-0 tune reproduces the mini-jet correlation structures best, which is why it is our choice. Its limitation though is a relatively small multiplicity reach, smaller than the one observed in data. As a result the MC calculation for our highest multiplicity range is less reliable—this is reflected in the systematic error.

Analyzing the shape of the underlying event correlation for identical particle pairs in MC is important; however, it does not ensure that the behavior of the correlation at very low q is reproduced well in MC. We compared the identical particle MC and data in the large q region, where the femtoscopic effect is expected to disappear, and found them to be very similar in all multiplicity/ k_T . However, if the mini-jet hypothesis is correct, the same phenomenon causes similar correlations to appear for nonidentical pions. The magnitude is expected to be higher than for identical pions because it is easier to produce an oppositely-charged pair from a fragmenting mini-jet than it is to create an identically-charged pair, due to local charge conservation. Moreover, the femtoscopic effect for nonidentical pions comes from the Coulomb interaction only. It is limited to very low q , below 0.1 GeV/ c . It is therefore possible to test the low- q behavior of the mini-jet correlation with such correlations. In Fig. 8 we show the measured $\pi^+\pi^-$ correlation functions, in selected

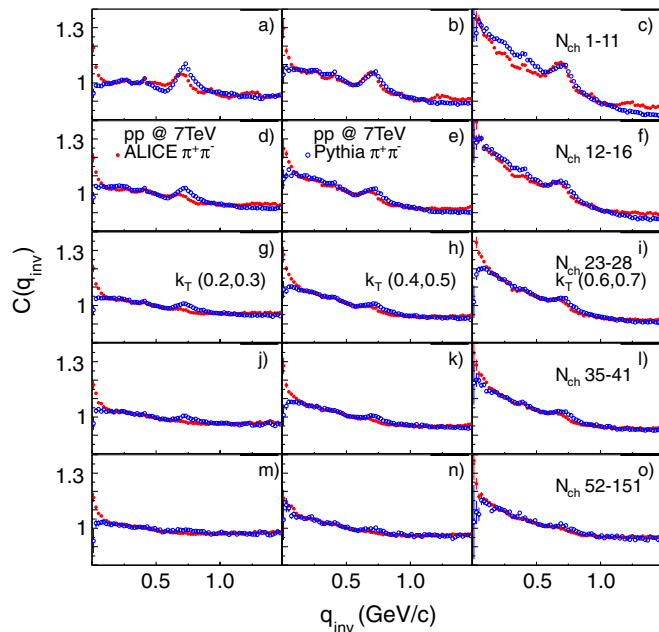


FIG. 8 (color online). Comparison of the correlation functions for $\pi^+\pi^-$ pairs at $\sqrt{s} = 7$ TeV (closed symbols) to the PYTHIA MC simulations (open symbols), in selected multiplicity and k_T intervals. The plot is made as a function of q_{inv} instead of q_{LCMS} so that the resonance peaks are better visible.

multiplicity/ k_T ranges, compared to the corresponding correlations from the same MC sample which was used to produce correlations in Fig. 7. The underlying event long-range correlation is well reproduced in the MC. We see some deviation in the lowest multiplicity range, which is taken into account in the systematic error estimation. At larger multiplicities the strength of the correlation is well reproduced. By comparing the three-dimensional function in SH we checked that the shape in three-dimensional q space is also in agreement between data and MC. The magnitude for nonidentical pions is slightly bigger than for identical pions, as expected. The femtoscopic Coulomb effect at $q < 0.1$ GeV/ c is also visible. Another strong effect, even dominating at low multiplicity, are the peaks produced by the correlated pairs of pions coming from strong resonance decays. They do appear in the MC as well, but they are shifted and have different magnitude. This is the effect of the simplified treatment of resonance decays in PYTHIA, where phase space and final state re-scattering are not taken into account. By analyzing some of the correlation functions in Fig. 8 we were able to identify signals from at least the following decays: two-body ρ , f_0 , and f_2 mesons decays, three-body ω meson decay, and also possibly η meson two-body decay. Some residual K_S^0 weak decay pairs, which are not removed by our DCA selection, can also be seen. All of these contribute through the full q range (0.0, 1.2) GeV/ c . This fact, in addition to the stronger mini-jet contribution to nonidentical (as compared to identical) correlations, makes the nonidentical correlation not suitable for the background estimation for identical pion pairs. We also note that there appears to be very rich physics content in the analysis of resonances decaying strongly in the $\pi^+\pi^-$ channel; however, we leave the investigation of this topic for separate studies.

The study of the $\pi^+\pi^-$ correlations confirms that the MC generator of choice reproduces the underlying event structures also at low q . We found that they are adequately described by a Gaussian in the LCMS for the C_0^0 component. The dashed lines in Fig. 7 show the fit of this form to the correlation in MC. The results of this fit, taken bin-by-bin for all multiplicity/ k_T ranges, are the input to the fitting procedure described in Sec. III D. Similarly, the observed C_0^0 correlation can be characterized well by a Gaussian, with the magnitude of -0.01 or less and a peak around $q = 0.5$ GeV/ c with a width of 0.25–0.5 GeV/ c . We proceed in the same way as for C_0^0 ; we fit the MC correlation structures with this functional form and take the results as fixed input parameters in the fitting of the measured correlations.

D. Fitting the correlation function

Having qualitatively analyzed the correlation functions themselves we move to the quantitative analysis. The femtoscopic part of the correlation function is defined theoretically via the Koonin-Pratt equation [30,31]:

$$C(\vec{q}, \vec{k}) = \int S(\mathbf{r}, \vec{q}, \vec{k}) |\Psi(\mathbf{r}, \vec{q})|^2 d^4\mathbf{r}, \quad (2)$$

where \vec{q} is the pair 3-momenta difference (the fourth component is not independent for pairs of identical pions since masses of particles are fixed), \vec{k} is the pair total momentum, \mathbf{r} is the pair space-time separation at the time when the second particle undergoes its last interaction, Ψ is the wave function of the pair, and S is the pair separation distribution. The aim in the quantitative analysis of the correlation function is to learn as much as possible about S from the analysis of the measured C . The correlation function C is, in the most general form, a six-dimensional object. We reduce the dimensionality to 3 by factorizing out the pair momentum k . We do not study the dependence on the longitudinal component of k in this work. The dependence on the transverse component of k is studied via the k_T binning, introduced in Sec. II. We assume that S is independent of k inside each of the k_T ranges. We also note that for identical pions the emission function S is a convolution of two identical single particle emission functions S_1 .

In order to perform the integral in Eq. (2) we must postulate the functional form of S or S_1 . We assume that S does not depend on q . The first analysis is performed with S_1 as a three-dimensional ellipsoid with Gaussian density profile. This produces S , which is also a Gaussian (with σ larger by a factor of $\sqrt{2}$):

$$S(r_o, r_s, r_l) = N \exp\left(-\frac{r_o^2}{4R_{\text{out}}^G} - \frac{r_s^2}{4R_{\text{side}}^G} - \frac{r_l^2}{4R_{\text{long}}^G}\right), \quad (3)$$

where R_{out}^G , R_{side}^G , and R_{long}^G are pion femtoscopic radii, also known as ‘‘Hanbury Brown and Twiss radii’’ or ‘‘homogeneity lengths’’, and r_o , r_s , and r_l are components of the pair separation vector. For identical charged pions Ψ should take into account the proper symmetrization, as well as Coulomb and strong interactions in the final state. In the case of the analysis shown in this work, with pions emitted from a region with the expected size not larger than 2–3 fm, the strong interaction contribution is relatively small and can be neglected [32]. The influence of the Coulomb interaction is approximated with the Bowler-Sinyukov method. It assumes that the Coulomb part can be factorized out from Ψ and integrated independently. There are well-known limitations to this approximation, but they have minor influence for the analysis shown in this work. With these assumptions Ψ is a sum of two plane waves modified by a proper symmetrization. By putting Eq. (3) into Eq. (2) the integration can be done analytically and yields the quantum statistics-only correlation C_{qs} :

$$C_{qs} = 1 + \lambda \exp(-R_{\text{out}}^G{}^2 q_{\text{out}}^2 - R_{\text{side}}^G{}^2 q_{\text{side}}^2 - R_{\text{long}}^G{}^2 q_{\text{long}}^2), \quad (4)$$

where λ is the fraction of correlated pairs for which both pions were correctly identified. The three-dimensional

correlation function is then modified with the Bowler-Sinyukov formula to obtain the complete femtoscopic component of the correlation C_f :

$$C_f(\vec{q}) = (1 - \lambda) + \lambda K(q_{\text{inv}}) [1 + \exp(-R_{\text{out}}^G{}^2 q_{\text{out}}^2 - R_{\text{side}}^G{}^2 q_{\text{side}}^2 - R_{\text{long}}^G{}^2 q_{\text{long}}^2)], \quad (5)$$

where K is the Coulomb like-sign pion pair wave function squared averaged over the Gaussian source with a radius of 1 fm. Changing this radius within the range of values measured in this work has negligible effect on the extracted radii. Equation (5) describes properly the femtoscopic part of the two-pion correlation function. However, in the previous section we have shown that our experimental functions also contain other, nonfemtoscopic correlations. We studied them in all multiplicity/ k_T ranges and found that they can be generally described by a combination of an angle-averaged Gaussian in the LCMS plus a small Gaussian deviation in the C_2^0 component:

$$B(\vec{q}_{\text{LCMS}}) = A_h \exp(-|\vec{q}_{\text{LCMS}}|^2 A_w^2) + B_h \exp\left(\frac{-(|\vec{q}_{\text{LCMS}}| - B_m)^2}{2B_w^2}\right) (3\cos^2(\theta) - 1), \quad (6)$$

where A_h , A_w , B_h , B_m , and B_w are parameters. They are obtained, bin-by-bin, from the fit to the MC simulated correlation functions shown in Fig. 7. They are fixed in the procedure of fitting the data. The final functional form that is used for fitting is then

$$C(q_{\text{out}}, q_{\text{side}}, q_{\text{long}}) = N C_f(q_{\text{out}}, q_{\text{side}}, q_{\text{long}}) B(q_{\text{out}}, q_{\text{side}}, q_{\text{long}}), \quad (7)$$

where N is the overall normalization. Projections of the Cartesian representation of the correlation functions, shown in Figs. 1 and 4, are normalized with this factor. Function (7) is used to fit both the SH and the Cartesian representation of the three-dimensional correlations.

In Fig. 9 an example of the fit to one of our correlation functions is shown. The SH representation of the data is shown as points; the result of the fit is a black dashed line. The femtoscopic component is shown as a blue dotted line, and the nonfemtoscopic background as green dash-dotted line. The correlation function in this range has significant contribution from the background and is reasonably reproduced by the fit. At $q < 0.1$ GeV/ c the fit misses the data points in C_0^0 at very low q and, as a consequence, in C_2^2 as well. This excess correlation suggests that the assumed Gaussian form can only be used to extract the overall size of the system, not the details of the shape. A different functional form, with more pronounced structures at large emission separations, is needed to fully describe this excess. An attempt to find such a form is described in detail in Sec. IV C. Here we proceed with the Gaussian assumption, as it is standard in the field and it is necessary to use it for

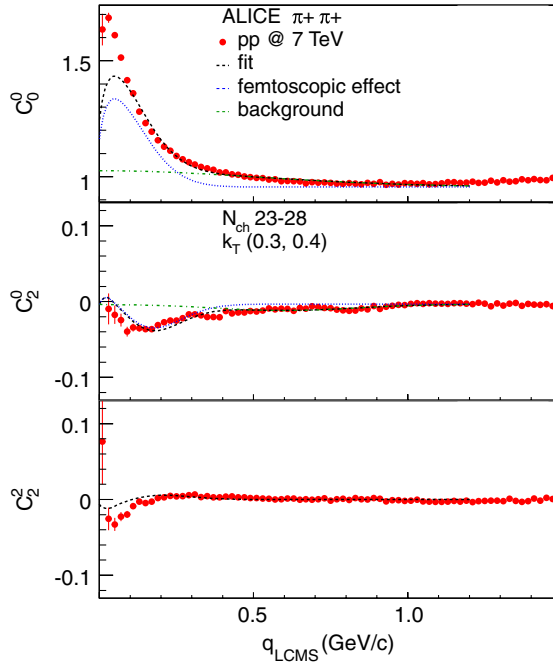


FIG. 9 (color online). Moments of the SH decomposition of the correlation functions for events with $23 \leq N_{\text{ch}} \leq 28$ and pairs with $0.3 < k_T < 0.4$ GeV/c. The dashed line shows the Gaussian fit, the dash-dotted line shows the background component, the dotted line shows the femtoscopic component.

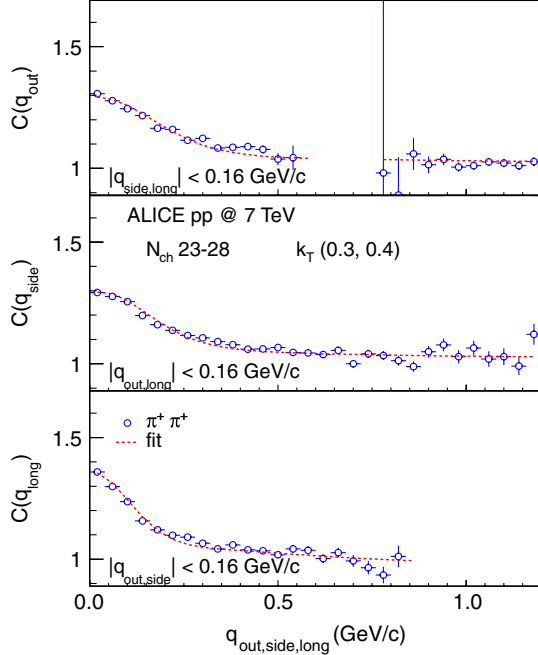


FIG. 10 (color online). Projections of the three-dimensional Cartesian representations of the correlation functions for events with $23 \leq N_{\text{ch}} \leq 28$ and pairs with $0.3 < k_T < 0.4$ GeV/c. To project onto one q component, the others are integrated over the range 0–0.16 GeV/c. Dashed lines show analogous projections of the Gaussian fit.

comparisons to other experiments and heavy-ion data. In Fig. 10 the same correlation is shown as projections of the three-dimensional Cartesian representation. The other q components are integrated over the range of 0–0.16 GeV/c. The fit, shown as lines, is similarly projected. In this plot the fit does not describe the shape of the correlation perfectly; however, the width is reasonably reproduced.

IV. FIT RESULTS

A. Results of the three-dimensional Gaussian fits

We fitted all 72 correlation functions (4 + 8 multiplicity ranges for two energies times 6 k_T ranges) with Eq. (7). We show the resulting femtoscopic radii in Fig. 11 as a function of k_T . The strength of the correlation λ is relatively independent of k_T , is 0.55 for the lowest multiplicity, decreases monotonically with multiplicity, and reaches the value of 0.42 for the highest multiplicity range. The

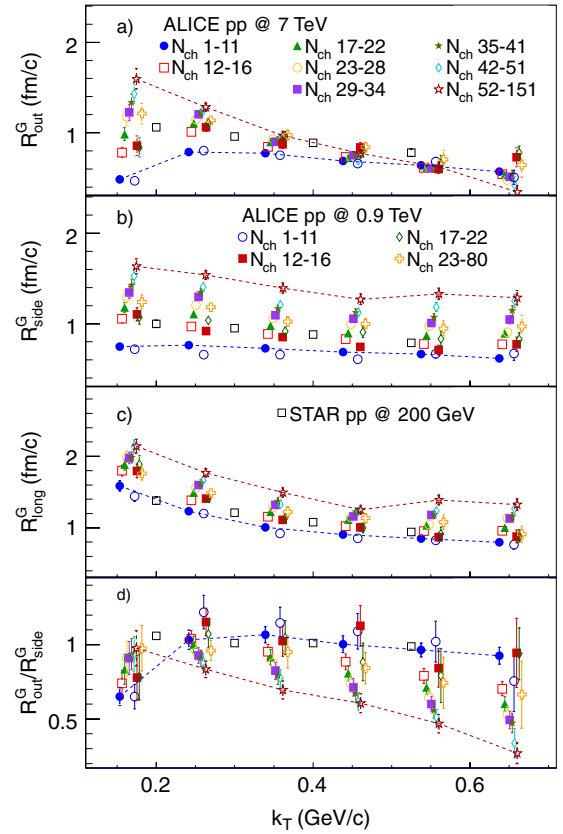


FIG. 11 (color online). Parameters of the three-dimensional Gaussian fits to the complete set of the correlation functions in 8 ranges in multiplicity and 6 in k_T for pp collisions at $\sqrt{s} = 7$ TeV, and 4 ranges in multiplicity and 6 in k_T for pp collisions at $\sqrt{s} = 0.9$ TeV. All points at given k_T bin should be at the same value of k_T , but we shifted them to improve visibility. Open black squares show values for pp collisions at $\sqrt{s} = 200$ GeV from STAR [10]. Lines connecting the points for lowest and highest multiplicity range were added to highlight the trends.

radii shown in the Fig. 11 are the main results of this work. Let us now discuss many aspects of the data visible in this figure.

First, the comparison between the radii for two energies, in the same multiplicity/ k_T ranges, reveals that they are universally similar at all multiplicities, all k_T 's, and all directions. This confirms what we have already seen directly in the measured correlation functions. The comparison to $\sqrt{s} = 200$ GeV pp collisions at RHIC is complicated by the fact that these data are not available in multiplicity ranges. The multiplicity reach at RHIC corresponds to a combination of the first three multiplicity ranges in our study. No strong change is seen between the RHIC and LHC energies. It shows that the space-time characteristics of the soft particle production in pp collisions are only weakly dependent on collision energy in the range between 0.9 TeV to 7 TeV, if viewed in narrow multiplicity/ k_T ranges. Obviously the $\sqrt{s} = 7$ TeV data have a higher multiplicity reach, so the minimum-bias (multiplicity/ k_T integrated) correlation function for the two energies is different.

Second, we analyze the slope of the k_T dependence. R_{long}^G falls with k_T at all multiplicities and both energies. R_{out}^G and R_{side}^G show an interesting behavior—at low multiplicity the k_T dependence is flat for R_{side}^G and for R_{out}^G it rises at low k_T and then falls again. For higher multiplicities both transverse radii develop a negative slope as multiplicity increases. At high multiplicity the slope is bigger for R_{out}^G , while R_{side}^G grows universally at all k_T 's while developing a smaller negative slope. The difference in the evolution of shapes of R_{out}^G and R_{side}^G is best seen in their ratio, shown in panel (d) of Fig. 11. At low multiplicities the ratio is close to 1.0, then it decreases monotonically with multiplicity. We note that a negative slope in R_{out}^G and R_{side}^G was universally observed in all heavy-ion measurements at RHIC energies and sometimes also at lower energies. It is interpreted as a signature of the existence of strong space-momentum correlations in the emission process, which arise naturally if matter behaves collectively, like a fluid [5,33]. The observation of the development, with increasing multiplicity, of such slope in pp collisions is consistent with the hypothesis that the larger the produced multiplicity, the more space-momentum correlations are present. They could come from a self-interacting and collective system or some other source; other measurements, e.g. inclusive transverse momentum spectra of identified particles as a function of multiplicity, are needed to draw conclusions about their nature. Nevertheless the possibility of the existence of strongly self-interacting collective system in high multiplicity pp collisions is exciting.

Third, all the measured radii grow with event multiplicity, in each k_T range separately. This is shown more clearly in Fig. 12, where we plot the radii as a function of $\langle dN_{\text{ch}}/d\eta \rangle^{(1/3)}$ (for our pp data we use the

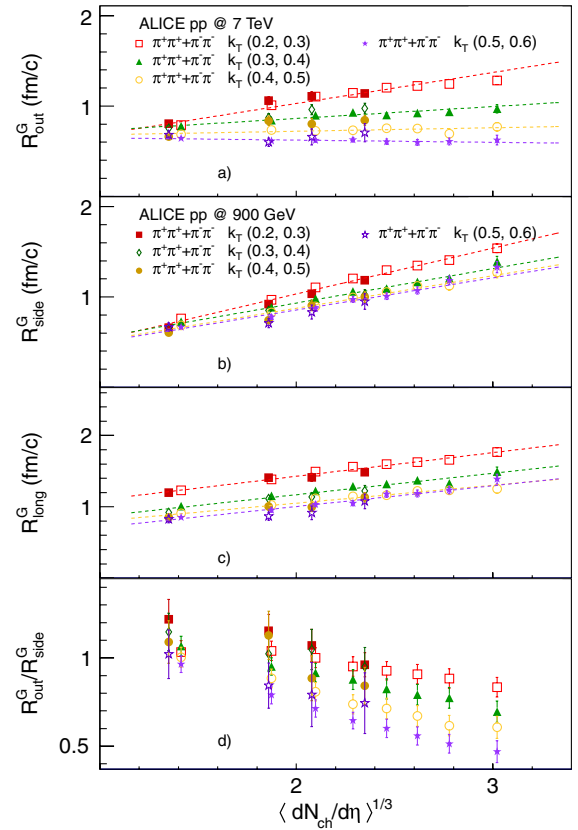


FIG. 12 (color online). Gaussian radii vs event multiplicity, for $\sqrt{s} = 0.9$ TeV and 7 TeV. Panel (a) shows R_{out}^G , (b) shows R_{side}^G , (c) shows R_{long}^G , and (d) shows $R_{\text{out}}^G/R_{\text{side}}^G$ ratio. Lines show linear fits to combined $\sqrt{s} = 0.9$ TeV and $\sqrt{s} = 7$ TeV points in each k_T range.

$\langle dN_{\text{ch}}/d\eta \rangle^{(1/3)}|_{N_{\text{ch}} \geq 1}$ given in Table I). Dashed lines show linear fits to the data, $\chi^2/N_{\text{d.o.f}}$ is below unity in all cases. R_{side}^G and R_{long}^G grow linearly with the cube root of charged-particle multiplicity, for all k_T ranges. Data, at both energies, follow the same scaling. For R_{out}^G the situation is similar for medium k_T ranges. The lowest k_T points show the strongest growth with multiplicity, while the highest hardly grows at all. That is the result of the strong change of the slope of k_T dependence with multiplicity, noted in the discussion of Fig. 11.

Similar multiplicity scaling was observed in heavy-ion collisions at RHIC energies and below. In Fig. 13 we compare our results to heavy-ion results from collision energies above 15 AGeV. This is the first time that one can directly compare pp and heavy-ion radii at the same $\langle dN_{\text{ch}}/d\eta \rangle$, as we measure $\langle dN_{\text{ch}}/d\eta \rangle$ comparable to the one in peripheral AuAu and CuCu collisions at RHIC. Since the value of the radius strongly depends on k_T , we carefully selected the results to have the same average $\langle k_T \rangle = 0.4$ GeV/c. The picture at other k_T 's is qualitatively similar. While both the heavy-ion and pp data scale linearly with $\langle dN_{\text{ch}}/d\eta \rangle^{(1/3)}$, the slope of the dependence is clearly different, for all directions. This is illustrated by the

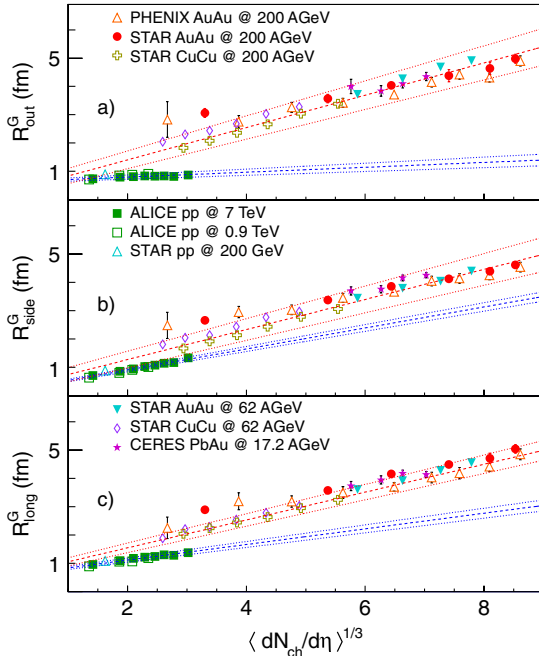


FIG. 13 (color online). Gaussian radii as a function of $\langle dN_{ch}/d\eta \rangle^{1/3}$, for $\sqrt{s} = 0.9$ TeV and 7 TeV, compared to the results from (heavy-) ion collisions at RHIC [35,36] and SPS [37]. Panel (a) shows R_{out}^G , (b) shows R_{side}^G , (c) shows R_{long}^G . All results are for $\langle k_T \rangle = 0.4$ GeV/c, except the values from the PHENIX experiment, which are at $\langle k_T \rangle = 0.45$ GeV/c. Dashed lines show linear fits, done separately to pp and heavy-ion data; dotted lines show the uncertainty in the fit.

dashed lines, which show linear fits, done separately to pp and (heavy-)ion data. The dotted lines show the range of dependencies allowed by the uncertainty of the fit. The pp results are systematically below the heavy-ion ones at similar multiplicity; therefore, the “universal” multiplicity scaling [5] observed in heavy-ion collisions does not hold for pp collisions at $\sqrt{s} = 0.9$ and 7 TeV. The pp radii do scale linearly with multiplicity but with a different slope. We also note that the linear scaling for (heavy-)ion data is only approximate, the $\chi^2/N_{d.o.f.}$ value for the fit presented here is significantly above unity, especially for R_{out}^G .

We speculate that the difference comes from a different way that the two types of collisions arrive at similar multiplicity. To produce a large number of particles in pp collision one needs a particularly energetic elementary collision that produces a lot of soft particles. The region where they are created is on the order of the incoming proton size and the growth of the size with multiplicity comes from further reinteraction between particles after they are born. In contrast, in heavy-ion collision we have many elementary nucleon scatterings, each of them producing initially a relatively low multiplicity. These scatterings are distributed inside the overlap region of the two nuclei, and this initial distribution influences the final observed size. In this picture, one would expect the

heavy-ion sizes to be larger than the ones observed in pp at the same multiplicity.

B. Systematic uncertainty

The correlation function is, to the first order, independent of the single particle acceptance and efficiency. We performed the analysis independently for many samples of data that naturally had single particle efficiencies different by up to 5%. We analyzed positive and negative pions separately, data at two magnetic field polarities, data from three different monthlong “LHC periods,” each of them having a slightly different detector setup. Two-particle correlations from all these analyzes were consistent within statistical errors.

We studied the effect of momentum resolution on the correlation peak with the MC simulation of our detector. At this low p_T , below 1 GeV/c, the momentum resolution for tracks reconstructed in the TPC is below 1%. This was confirmed by several methods, including the reconstruction of tracks from cosmic rays and comparison of the reconstructed K_S^0 mass peak position with the expected value. The smearing of single particle momenta does result in the smearing of the correlation peak: it makes it appear smaller and wider. We estimated that this changes the reconstructed radius by 1% for the femtoscopic size of 1 fm; the effect grows to 4% for the size of 2 fm, as it corresponds to a narrower correlation peak.

In contrast to single particle acceptance, the femtoscopic correlation function is sensitive to the two-track reconstruction effects, usually called “splitting” and “merging”. The splitting occurs when one track is mistakenly reconstructed as two. Both tracks have then very close momenta. This results in a sharp correlation peak at low relative momentum. We have seen such effects in the data, and we took several steps to remove them. First, the requirement that the track is simultaneously reconstructed in the TPC and ITS decreases splitting significantly. In addition, each cluster in the TPC is flagged as “shared” if it is used in the reconstruction of more than one track. The split tracks tend to produce pairs which share most of their clusters; therefore, we removed pairs that share more than 5% of the TPC clusters. We also look for configurations where a single track is split in two segments in the TPC, e.g. by the TPC central membrane or a TPC sector boundary. Such segments should be correctly connected in the tracking procedure to form a single track if the detector calibration is perfect. However, in a few rare cases this does not happen and a split track can appear. Such pairs would consist of two tracks that have a relatively small number of TPC clusters and they would rarely both have a cluster in the same TPC padrow. Therefore, we count, for each pair, the number of times that both tracks have a separate (nonshared) cluster in a TPC padrow. Pairs for which this number is low are removed. Both selections are applied in the same way to the signal and background

distributions. As a consequence, the fake low-momentum pairs from splitting are almost completely removed, and the remaining ones are concentrated in a very narrow relative momentum q range, corresponding essentially to the first correlation function bin. The inclusion of this bin has a negligible effect on the fitting result; hence, we do not assign any systematic error on the fitting values from these procedures.

Another two-track effect is merging, where two distinct tracks are reconstructed as one, due to finite detector space-point resolution. The ALICE detector was specifically designed to cope with the track densities expected in heavy-ion $Pb + Pb$ collisions, which are expected to be orders of magnitude higher than the ones measured in pp collisions. More specifically, the ITS detector granularity as well as TPC tracking procedure, which allows for cluster sharing between tracks, make merging unlikely. We confirmed with detailed MC simulation of our detector setup that merging, if it appears at all, would only affect the correlation function in the lowest q bin, which means that it would not affect the measured radii.

In summary, the systematic uncertainty on the raw measurement, the correlation function itself, is small.

The most significant systematic uncertainty on the extracted radii comes from the fact that we rely on the MC simulation of the mini-jet underlying event correlations. We fix the parameters of the B function in Eq. (7) by fitting it to the correlations obtained from the MC generated events. We confirmed with the analysis of the nonidentical $\pi^+ \pi^-$ pairs that our Monte-Carlos of choice, the Perugia-0 tune of the PYTHIA 6 model, and the PHOJET model reproduce the height and the width of the “mini-jet peak with an accuracy better than 10%, except the first multiplicity range where the differences go up to 20% for the highest k_T range. We performed the fits to the correlation function varying the parameters A_h and B_h of the B function by $\pm 10\%$, and A_w by 5%. The fit values for the case when A_h , B_h are decreased and A_w is increased (corresponding to smaller mini-jet correlations) are systematically below the standard values. For larger mini-jet correlations they are systematically above. The resulting relative systematic uncertainty on all radii is given in Table II. The error is independent of multiplicity, except for the first and last

TABLE II. Systematic uncertainty coming from varying mini-jet background height/width by 10%/5% up/down.

k_T (GeV/c)	ΔR_{out}^G %	ΔR_{side}^G %	ΔR_{long}^G %
(0.13, 0.2)	4	1	2
(0.2, 0.3)	4	3	2
(0.3, 0.4)	4	3	2
(0.4, 0.5)	7	4	4
(0.5, 0.6)	9	4	4
(0.6, 0.7)	13	7	7

multiplicity ranges, where it is higher by 50%. This error is fully correlated between multiplicity/ k_T ranges.

Independently, we performed the fits with the PHOJET generator and fixed the parameters of B from them. The difference in the final fitted radii between PYTHIA and PHOJET background is taken as another component of the systematic error, shown in Table III.

Another effect, visible in Fig. 9, is that the traditional Gaussian functional form does not describe the shape of the correlation perfectly. As a result, the extracted radius depends on the range used in fitting. Generally, the larger the fitting range, the smaller the radius. We fixed our maximum fitting range to 1.2 GeV, which is sufficient to cover all correlation structures seen in data. We estimate that the remaining systematic uncertainty coming from the fitting range is shown in Table IV

We always performed all fits separately to correlations for $\pi^+ \pi^+$ and $\pi^- \pi^-$ pairs. They are expected to give the same source size; therefore the difference between them is taken as an additional component of the systematic uncertainty.

We used two independent representations of the three-dimensional correlation functions: the “Cartesian” one uses standard three-dimensional histograms to store the signal and the mixed background. The SH one uses sets of one-dimensional histograms to store the SH components plus one three-dimensional histogram to store the covariances between them (see Sec. III A for more details). The fitting of the two representations, even though it uses the same mathematical formula (7), is different from the technical point of view. The SH procedure is more robust against holes in the acceptance [24], visible in our data, e.g. in Fig. 3. In an ideal case both procedures should produce identical fit results; therefore, we take the difference between the radii obtained from the two procedures as an estimate of the systematic uncertainty incurred by the fitting procedure itself. The error is shown in Table V as a function of k_T . The large error at low k_T is coming from the fact that the two procedures are sensitive to the holes in the acceptance in a different way. It reflects the experimental fact that, in these k_T ranges, pairs in certain kinematic regions are not measured; therefore, the femtoscopic radius cannot be obtained with better accuracy. In the highest k_T

TABLE III. Systematic uncertainty coming from comparing the fit values with background obtained from PHOJET and PYTHIA simulations.

k_T (GeV/c)	ΔR_{out}^G %	ΔR_{side}^G %	ΔR_{long}^G %
(0.13, 0.2)	7	4	2
(0.2, 0.3)	1	1	4
(0.3, 0.4)	1	1	4
(0.4, 0.5)	7	2	4
(0.5, 0.6)	7	3	4
(0.6, 0.7)	10	6	7

TABLE IV. Systematic uncertainty coming from varying the maximum fit range.

k_T (GeV/ c)	ΔR_{out}^G %	ΔR_{side}^G %	ΔR_{long}^G %
(0.13, 0.2)	3	2	1
(0.2, 0.3)	4	4	3
(0.3, 0.4)	7	5	3
(0.4, 0.5)	7	5	1
(0.5, 0.6)	7	4	3
(0.6, 0.7)	10	4	4

TABLE V. Systematic uncertainty coming from comparing the fits to two independent three-dimensional correlation function representations.

k_T (GeV/ c)	ΔR_{out}^G %	ΔR_{side}^G %	ΔR_{long}^G %
(0.13, 0.2)	9	5	15
(0.2, 0.3)	9	7	7
(0.3, 0.4)	4	2	2
(0.4, 0.5)	6	2	4
(0.5, 0.6)	8	3	4
(0.6, 0.7)	18	6	12

range the mini-jet underlying correlation is highest and broadest. If our simple phenomenological parametrization of it does not perfectly describe its behavior in full three-dimensional space, it can affect differently a fit in the Cartesian and SH representations.

In summary, the combined systematic error is 10% for all k_T and multiplicity ranges except the ones at the lower and upper edge. It is 20% for the lowest and highest k_T and for the lowest and highest multiplicity range at each collision energy. It is also never smaller than 0.1 fm.

C. Non-Gaussian fits

In the discussion of Fig. 9 we note that the measured correlation function is not perfectly reproduced by a three-dimensional Gaussian fit. In our previous work [14] and in the work of the CMS collaboration [15] it was noted that the shape of the one-dimensional correlation in the Pair Rest Frame is better described by an exponential shape. Also, model studies [34] suggest that pion production at these energies has large contribution from strongly decaying resonances. This is confirmed by the observation of significant resonance peaks in the $\pi^+ \pi^-$ correlation functions, seen e.g. in Fig. 8. Resonances decay after random time governed by the exponential decay law, which transforms into an exponential shape in space via the pair velocity. By definition pair velocity exists in the out and long direction and vanishes in *side*. It is then reasonable to attempt to fit the correlation with a functional form other than a simple Gaussian, at least for the *out* and *long* components.

If we keep the assumption that the emission function factorizes into the out, side, and long directions, we can write a general form of the pair emission function:

$$S(\mathbf{r}) = S_o(r_o)S_s(r_s)S_l(r_l). \quad (8)$$

We can independently change each component. We stress, however, that only for a Gaussian there is an analytically known correspondence between the pair separation distribution S and single particle emission function S_1 . Two commonly used forms of S are exponential and Lorentzian. They have the desired feature that the integration in Eq. (2) can be analytically carried out and produce a Lorentzian and exponential in C , respectively. In order to select the proper combination of functional forms we seek guidance from models. They suggest that at least in the out and long direction the emission function is not Gaussian and in some cases seems to be well described by a Lorentzian. We performed a study of all 27 combinations of the fitting functions for selected multiplicity/ k_T ranges. We found that universally the out correlation function was best described by an exponential, corresponding to Lorentzian emission function, which agrees with model expectations. In contrast, the side direction is equally well described by a Gaussian or a Lorentzian; we chose the former because the Lorentzian correlation function would correspond to exponential pair emission function with a sharp peak at 0. We deem this unlikely, given that the models do not produce such shapes. In long, the correlation function is not Gaussian; hence, we chose the exponential shape in C for the fit. In conclusion, we postulate that the source has the following shape:

$$S(\mathbf{r}) = \frac{1}{r_o^2 + R_{\text{out}}^E} \exp\left(-\frac{r_s^2}{4R_{\text{side}}^G}\right) \frac{1}{r_l^2 + R_{\text{long}}^E}, \quad (9)$$

which corresponds to the following form of the femtoscopic part of the correlation function formula:

$$C_f = 1 + \lambda \exp(-\sqrt{R_{\text{out}}^E}^2 q_{\text{out}}^2 - R_{\text{side}}^G q_{\text{side}}^2 - \sqrt{R_{\text{long}}^E}^2 q_{\text{long}}^2). \quad (10)$$

In Figs. 14 and 15 we show an example of the exponential-Gaussian-exponential fit to the correlation functions at multiplicity $23 \leq N_{\text{ch}} \leq 28$ and k_T in (0.3, 0.4) GeV/ c . In the SH representation we see improvements over the Gaussian fit from Fig. 9. The behavior in C_0^0 at low q is now well described. In C_2^2 the ‘‘wobble’’ in the correlation is also reproduced—this is possible because the functional forms for the out and side directions are now different. In the Cartesian projections the improvement is also seen; however, it is not illustrated as clearly as in the SH.

We then proceed with the fitting of the full set of 72 correlation functions. The resulting fit parameters are summarized in Fig. 16. The quality of the fit (judged by the value of χ^2/N_{dof}) is better than for the three-dimensional

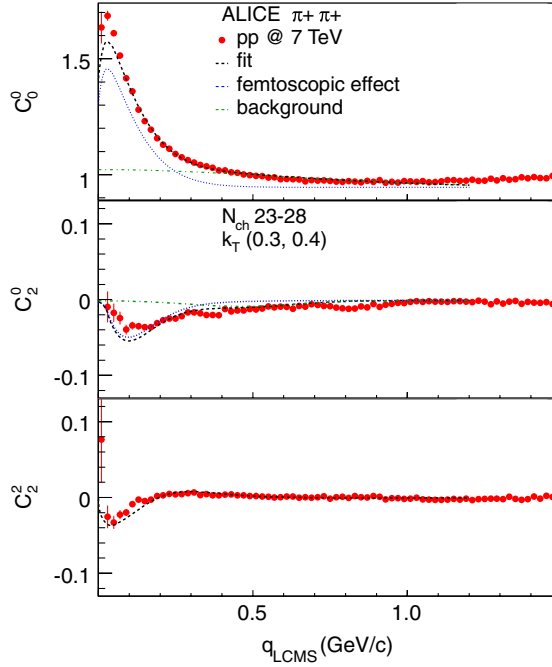


FIG. 14 (color online). Exponential-Gaussian-exponential fit example for events with $23 \leq N_{\text{ch}} \leq 28$, pairs with $0.3 < k_T < 0.4$ GeV/c SH representation. Dotted line shows the femtoscopic component, dash-dotted line shows the background, the dashed line shows the full fit.

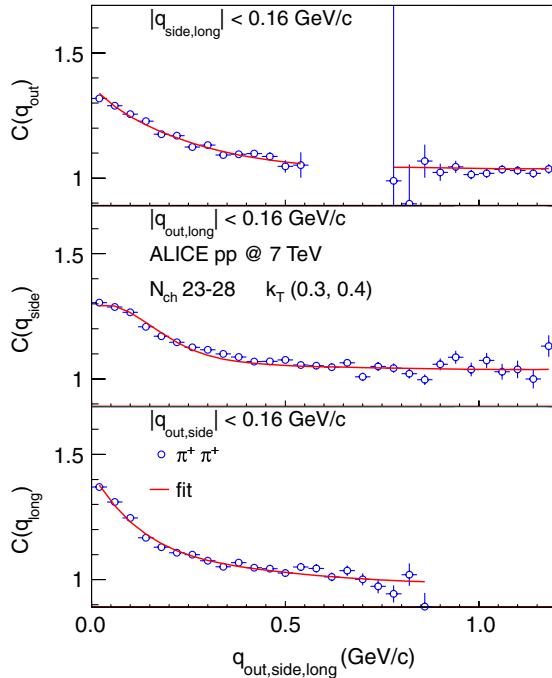


FIG. 15 (color online). Exponential-Gaussian-exponential fit example for events with $23 \leq N_{\text{ch}} \leq 28$, pairs with $0.3 < k_T < 0.4$ GeV/c. One-dimensional projections of the Cartesian representation are shown, the other q components were integrated in the range 0–0.16 GeV/c.

Gaussian fit. The λ parameter is higher by up to 0.2, as compared to the pure Gaussian fit, reflecting the fact that the new functional form accounts for the pairs contributing to the narrow correlation peak at small q . The resulting exponential radii cannot be directly compared in magnitude to the Gaussian radii from other experiments. However all the features seen in dependencies of the Gaussian radii on multiplicity and k_T are also visible here. This confirms that with a functional form that fits our correlation function well (better than a three-dimensional Gaussian) the physics message from the dependence of radii on multiplicity and k_T remains valid. The study of the fit functional form shows that the correlation does not have a Gaussian shape in out and long.

The R_{side}^G from this fit should be equal to the R_{side}^G from the three-dimensional Gaussian fit with two caveats. The first is the assumption that the emission function fully factorizes into separate functions for out, side, and long directions. In the fitting of the three-dimensional correlation functions the residual correlation between the value of the λ parameter and the values of the radii is often

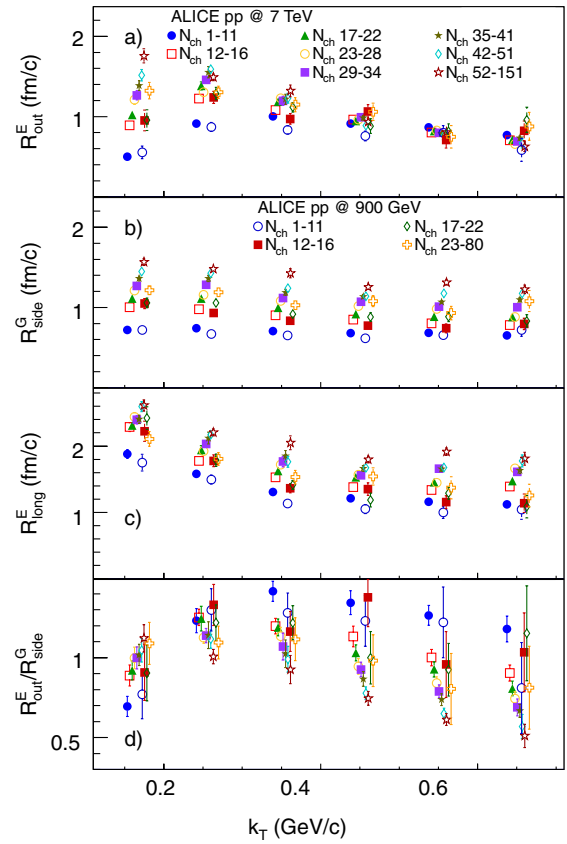


FIG. 16 (color online). Non-Gaussian fit radii [see Eq. (10)] as a function of pair momentum k_T for all multiplicity ranges and for two collision energies. Panel (a) shows R_{out}^E , panel (b) shows R_{side}^G , panel (c) shows R_{long}^E , panel (d) shows $R_{\text{out}}^E/R_{\text{side}}^G$ ratio. All points at given k_T bin should be at the same value of k_T , but we shifted them to improve visibility.

observed. We noted already that the non-Gaussian fit produces larger values of λ , so R_{side}^G could be affected. Nevertheless we observe very good agreement (within statistical errors for multiplicities above 16) between the R_{side}^G values from both fits, giving us additional confidence that the underlying assumptions in our fit are valid.

Similar conclusions can be drawn from the ratio of the $R_{\text{out}}^E/R_{\text{side}}^G$ for the more advanced functional form, shown in panel (d) of Fig. 16. Again, the picture seen for the Gaussian radii is confirmed; the higher the multiplicity of the collision and the collision energy, the lower the value of the ratio.

V. FITTING ONE-DIMENSIONAL CORRELATIONS

For completeness, we also repeated the one-dimensional study in Pair Rest Frame, using all the methods and fitting functions described in the previous work of ALICE [14]. The one-dimensional correlation functions are fit with the standard Gaussian form, modified with the approximate Bowler-Sinyukov formula to account for the Coulomb interaction between charged pions:

$$C(q_{\text{inv}}) = [(1 - \lambda) + \lambda K(q_{\text{inv}})(1 + \exp(-R_{\text{inv}}^2 q_{\text{inv}}^2))] B(q_{\text{inv}}), \quad (11)$$

where K is the Coulomb function averaged over a spherical source of the size 1.0 fm, R_{inv} is the femtoscopic radius, and B is the function describing the nonfemtoscopic background. In Fig. 17 we plot the Gaussian one-dimensional invariant radius as a function of multiplicity and k_T . The closed and open stars are the results from our earlier work, which are consistent with the more precise results from this analysis. The systematic error is on the order of 10% and is

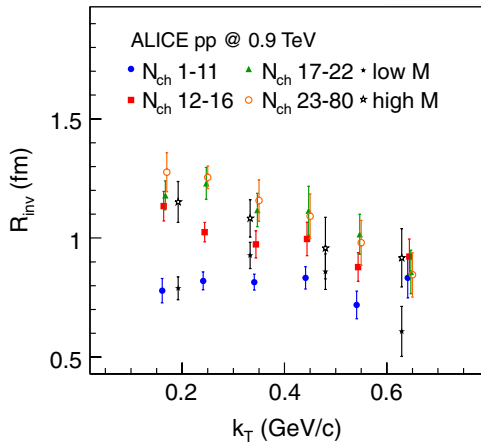


FIG. 17 (color online). One-dimensional R_{inv} radius for all multiplicity and k_T ranges for the $\sqrt{s} = 0.9$ TeV data. The points for different multiplicities were slightly shifted in k_T for clarity. The systematic error, typically on the order of 10% is not shown [16]. Closed and open stars show the previously published result from [14] for two ranges of the multiplicity M .

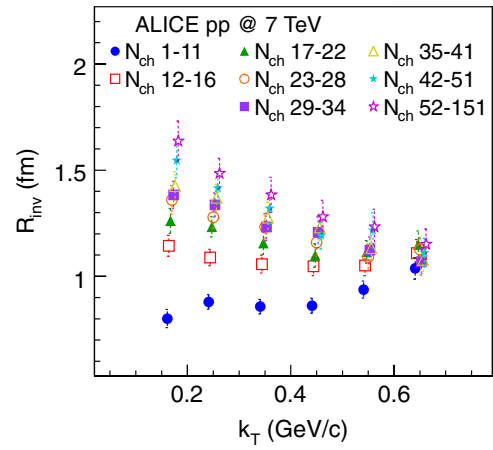


FIG. 18 (color online). One-dimensional R_{inv} radius versus multiplicity and k_T for the $\sqrt{s} = 7$ TeV data. The points for different multiplicities were slightly shifted in k_T for clarity. The systematic error, typically on the order of 10% is not shown [16].

now dominating the precision of the measurement. At $\sqrt{s} = 0.9$ TeV we see that, for the lowest multiplicity, the radius is not falling with k_T , while it develops a slope as one goes to higher multiplicity. The one-dimensional analysis is consistent with the three-dimensional measurement—one needs to take into account that when going from the LCMS (three-dimensional measurement) to the PRF (one-dimensional measurement) it is necessary to boost the out radius by pair velocity, which is defined by k_T . Then, one averages the radii in three directions to obtain the one-dimensional R_{inv} .

In Fig. 18 we show the same analysis performed for the $\sqrt{s} = 7$ TeV data. The radii are again comparable at the same multiplicity/ k_T range. In addition, as one goes to higher multiplicities, the k_T dependence of R_{inv} is getting more pronounced. The results are again consistent with the three-dimensional analysis.

VI. SUMMARY

In summary, ALICE measured two-pion correlation functions in pp collisions at $\sqrt{s} = 0.9$ TeV and at $\sqrt{s} = 7$ TeV at the LHC. The analysis was performed in multiplicity and pair transverse momentum ranges. When viewed in the same multiplicity and pair momentum range, correlation functions at the two collision energies are similar.

The correlations are analyzed quantitatively by extracting the emission source sizes in three dimensions: outward, sideward, and longitudinal. The longitudinal size shows expected behavior. It decreases with pair momentum and increases with event multiplicity, consistent with all previous measurements in elementary and heavy-ion collisions. The transverse sizes show more complicated behavior. The sideward radius grows with multiplicity

and has a negative correlation with pair momentum. The outward radius at the lowest multiplicity is small for the lowest k_T , increases for larger k_T , and then decreases. As the multiplicity grows the shape of the k_T dependence gradually changes to one monotonically falling with k_T . The resulting ratio of outward to sideward radii gets smaller as multiplicity grows. Similar dependencies in heavy-ion collisions were interpreted as signatures of the collective behavior of matter. One possible interpretation of the results in this work is that as one moves towards pp collisions producing high multiplicity of particles, similar collectivity develops. More experimental and theoretical information is needed to address this intriguing possibility.

The upper range of multiplicities produced in pp collisions at $\sqrt{s} = 7$ TeV is comparable to the multiplicities measured in peripheral heavy-ion collisions at RHIC. When plotted versus $\langle dN_{ch}/d\eta \rangle^{(1/3)}$ the radii in pp show linear scaling but with different slope and offset than those observed in heavy-ion collisions. Therefore our observations violate the universal $\langle dN_{ch}/d\eta \rangle^{(1/3)}$ scaling. This proves that the final observed particle multiplicity is not the only scaling variable in the system and the initial geometry must be taken into account in any scaling arguments.

The analysis is complicated by the existence of the long-range underlying event correlations. We assume these are the mini-jet structures which are visible at values of p_t as low as 0.5 GeV/ c . The Monte-Carlo studies are consistent with such a hypothesis and are used to parametrize and take into account the influence of mini-jets on the fitted femtoscopic radii. Studies of the $\pi^+ \pi^-$ correlations are also consistent with such hypothesis. Nevertheless, the need to account for this effect remains the main source of the systematic error.

Finally, the detailed analysis of the correlation reveals that the three-dimensional Gaussian describes the measurement only approximately. A better shape, exponential-Gaussian-exponential, is postulated, based on Monte-Carlo studies, and is found to better agree with the data. The resulting radii and their behavior versus event multiplicity and pair momentum are fully consistent with the one obtained with the Gaussian approximation.

ACKNOWLEDGMENTS

The ALICE Collaboration would like to thank all its engineers and technicians for their invaluable contributions to the construction of the experiment and the CERN accelerator teams for the outstanding performance of the LHC complex. The ALICE Collaboration acknowledges the following funding agencies for their support in building and running the ALICE detector: Calouste Gulbenkian

Foundation from Lisbon and Swiss Fonds Kidagan, Armenia; Conselho Nacional de Desenvolvimento Científico e Tecnológico (CNPq), Financiadora de Estudos e Projetos (FINEP), Fundação de Amparo à Pesquisa do Estado de São Paulo (FAPESP); National Natural Science Foundation of China (NSFC), the Chinese Ministry of Education (CMOE) and the Ministry of Science and Technology of China (MSTC); Ministry of Education and Youth of the Czech Republic; Danish Natural Science Research Council, the Carlsberg Foundation and the Danish National Research Foundation; The European Research Council under the European Community's Seventh Framework Programme; Helsinki Institute of Physics and the Academy of Finland; French CNRS-IN2P3, the "Region Pays de Loire," "Region Alsace," "Region Auvergne," and CEA, France; German BMBF and the Helmholtz Association; Greek Ministry of Research and Technology; Hungarian OTKA and National Office for Research and Technology (NKTH); Department of Atomic Energy and Department of Science and Technology of the Government of India; Istituto Nazionale di Fisica Nucleare (INFN) of Italy; MEXT Grant-in-Aid for Specially Promoted Research, Japan; Joint Institute for Nuclear Research, Dubna; National Research Foundation of Korea (NRF); CONACYT, DGAPA, México, ALFA-EC and the HELEN Program (High-Energy physics Latin-American-European Network); Stichting voor Fundamenteel Onderzoek der Materie (FOM) and the Nederlandse Organisatie voor Wetenschappelijk Onderzoek (NWO), Netherlands; Research Council of Norway (NFR); Polish Ministry of Science and Higher Education; National Authority for Scientific Research-NASR (Autoritatea Națională pentru Cercetare Științifică - ANCS); Federal Agency of Science of the Ministry of Education and Science of Russian Federation, International Science and Technology Center, Russian Academy of Sciences, Russian Federal Agency of Atomic Energy, Russian Federal Agency for Science and Innovations and CERN-INTAS; Ministry of Education of Slovakia; CIEMAT, EELA, Ministerio de Educación y Ciencia of Spain, Xunta de Galicia (Consellería de Educación), CEADEN, Cubaenergía, Cuba, and IAEA (International Atomic Energy Agency); The Ministry of Science and Technology and the National Research Foundation (NRF), South Africa; Swedish Research Council (VR) and Knut & Alice Wallenberg Foundation (KAW); Ukraine Ministry of Education and Science; United Kingdom Science and Technology Facilities Council (STFC); The United States Department of Energy, the United States National Science Foundation, the State of Texas, and the State of Ohio.

- [1] Z. Fodor and S. D. Katz, *J. High Energy Phys.* **03** (2002) 014.
 [2] G. Goldhaber, S. Goldhaber, W.-Y. Lee, and A. Pais, *Phys. Rev.* **120**, 300 (1960).
 [3] W. Kittel, *Acta Phys. Pol. B* **32**, 3927 (2001).
 [4] G. Alexander, *Rep. Prog. Phys.* **66**, 481 (2003).
 [5] M. Lisa, S. Pratt, R. Soltz, and U. Wiedemann, *Annu. Rev. Nucl. Part. Sci.* **55**, 357 (2005).
 [6] D. Hardtke and S. A. Voloshin, *Phys. Rev. C* **61**, 024905 (2000).
 [7] S. Pratt, *Nucl. Phys. A* **830**, 51c (2009).
 [8] L. Lonnblad and T. Sjostrand, *Eur. Phys. J. C* **2**, 165 (1998).
 [9] Z. Chajecski, *Acta Phys. Pol. B* **40**, 1119 (2009).
 [10] M. M. Aggarwal *et al.* (STAR), *Phys. Rev. C* **83**, 064905 (2011).
 [11] G. Paic and P. Skowronski, *J. Phys. G* **31**, 1045 (2005).
 [12] P. Bozek, *Acta Phys. Pol. B* **41**, 837 (2010).
 [13] K. Werner, I. Karpenko, T. Pierog, M. Bleicher, and K. Mikhailov, *Phys. Rev. C* **83**, 044915 (2011).
 [14] K. Aamodt *et al.* (ALICE), *Phys. Rev. D* **82**, 052001 (2010).
 [15] V. Khachatryan *et al.* (CMS), *Phys. Rev. Lett.* **105**, 032001 (2010).
 [16] The Durham HepData Project <http://durpdg.dur.ac.uk>.
 [17] K. Aamodt *et al.* (ALICE), *JINST* **3**, S08002 (2008).
 [18] K. Aamodt *et al.* (ALICE), *Eur. Phys. J. C* **68**, 345 (2010).
 [19] G. I. Kopylov, *Phys. Lett. B* **50**, 472 (1974).
 [20] S. Pratt, *Phys. Rev. D* **33**, 1314 (1986).
 [21] G. Bertsch, M. Gong, and M. Tohyama, *Phys. Rev. C* **37**, 1896 (1988).
 [22] D. A. Brown and P. Danielewicz, *Phys. Lett. B* **398**, 252 (1997).
 [23] Z. Chajecski and M. Lisa, *Braz. J. Phys.* **37**, 1057 (2007).
 [24] A. Kisiel and D. A. Brown, *Phys. Rev. C* **80**, 064911 (2009).
 [25] P. Danielewicz and S. Pratt, *Phys. Rev. C* **75**, 034907 (2007).
 [26] T. Sjostrand, S. Mrenna, and P. Z. Skands, *J. High Energy Phys.* **05** (2006) 026.
 [27] P. Z. Skands, [arXiv:0905.3418](https://arxiv.org/abs/0905.3418).
 [28] R. Engel, *Z. Phys. C* **66**, 203 (1995).
 [29] R. Engel and J. Ranft, *Phys. Rev. D* **54**, 4244 (1996).
 [30] S. E. Koonin, *Phys. Lett. B* **70**, 43 (1977).
 [31] S. Pratt, *Phys. Rev. Lett.* **53**, 1219 (1984).
 [32] R. Lednicky, *Phys. Part. Nucl.* **40**, 307 (2009).
 [33] S. V. Akkelin and Y. M. Sinyukov, *Phys. Lett. B* **356**, 525 (1995).
 [34] T. J. Humanic, *Phys. Rev. C* **76**, 025205 (2007).
 [35] S. S. Adler *et al.* (PHENIX), *Phys. Rev. Lett.* **93**, 152302 (2004).
 [36] B. I. Abelev *et al.* (STAR), *Phys. Rev. C* **80**, 024905 (2009).
 [37] D. Adamova *et al.* (CERES), *Nucl. Phys. A* **714**, 124 (2003).

K. Aamodt,¹ A. Abrahantes Quintana,² D. Adamová,³ A. M. Adare,⁴ M. M. Aggarwal,⁵ G. Aglieri Rinella,⁶ A. G. Agocs,⁷ S. Aguilar Salazar,⁸ Z. Ahammed,⁹ N. Ahmad,¹⁰ A. Ahmad Masoodi,¹⁰ S. U. Ahn,^{11,b} A. Akindinov,¹² D. Aleksandrov,¹³ B. Alessandro,¹⁴ R. Alfaro Molina,⁸ A. Alici,^{15,c} A. Alkin,¹⁶ E. Almaráz Aviña,⁸ T. Alt,¹⁷ V. Altini,^{18,d} S. Altinpinar,¹⁹ I. Altsybeev,²⁰ C. Andrei,²¹ A. Andronic,¹⁹ V. Anguelov,^{22,e} C. Anson,²³ T. Antičić,²⁴ F. Antinori,²⁵ P. Antonioli,²⁶ L. Aphecetche,²⁷ H. Appelshäuser,²⁸ N. Arbor,²⁹ S. Arcelli,¹⁵ A. Arend,²⁸ N. Armesto,³⁰ R. Arnaldi,¹⁴ T. Aronsson,⁴ I. C. Arsene,¹⁹ A. Asryan,²⁰ A. Augustinus,⁶ R. Averbeck,¹⁹ T. C. Awes,³¹ J. Äystö,³² M. D. Azmi,¹⁰ M. Bach,¹⁷ A. Badalà,³³ Y. W. Baek,^{11,b} S. Bagnasco,¹⁴ R. Bailhache,²⁸ R. Bala,^{34,f} R. Baldini Ferroli,³⁵ A. Baldisseri,³⁶ A. Baldit,³⁷ J. Bán,³⁸ R. Barbera,³⁹ F. Barile,¹⁸ G. G. Barnaföldi,⁷ L. S. Barnby,⁴⁰ V. Barret,³⁷ J. Bartke,⁴¹ M. Basile,¹⁵ N. Bastid,³⁷ B. Bathen,⁴² G. Batigne,²⁷ B. Batyunya,⁴³ C. Baumann,²⁸ I. G. Bearden,⁴⁴ H. Beck,²⁸ I. Belikov,⁴⁵ F. Bellini,¹⁵ R. Bellwied,^{46,g} E. Belmont-Moreno,⁸ S. Beole,³⁴ I. Berceanu,²¹ A. Bercuci,²¹ E. Berdermann,¹⁹ Y. Berdnikov,⁴⁷ L. Betev,⁶ A. Bhasin,⁴⁸ A. K. Bhati,⁵ L. Bianchi,³⁴ N. Bianchi,⁴⁹ C. Bianchin,²⁵ J. Bielčák,⁵⁰ J. Bielčiková,³ A. Bilandzic,⁵¹ E. Biolcati,^{6,h} A. Blanc,³⁷ F. Blanco,⁵² F. Blanco,⁵³ D. Blau,¹³ C. Blume,²⁸ M. Boccioni,⁶ N. Bock,²³ A. Bogdanov,⁵⁴ H. Bøggild,⁴⁴ M. Bogolyubsky,⁵⁵ L. Boldizsár,⁷ M. Bombara,⁵⁶ C. Bombonati,²⁵ J. Book,²⁸ H. Borel,³⁶ C. Bortolin,^{25,i} S. Bose,⁵⁷ F. Bossú,^{6,h} M. Botje,⁵¹ S. Böttger,²² B. Boyer,⁵⁸ P. Braun-Munzinger,¹⁹ L. Bravina,⁵⁹ M. Bregant,^{60,j} T. Breitner,²² M. Broz,⁶¹ R. Brun,⁶ E. Bruna,⁴ G. E. Bruno,¹⁸ D. Budnikov,⁶² H. Buesching,²⁸ O. Busch,⁶³ Z. Buthelezi,⁶⁴ D. Caffarri,²⁵ X. Cai,⁶⁵ H. Caines,⁴ E. Calvo Villar,⁶⁶ P. Camerini,⁶⁰ V. Canoa Roman,^{6,k} G. Cara Romeo,²⁶ F. Carena,⁶ W. Carena,⁶ F. Carminati,⁶ A. Casanova Díaz,⁴⁹ M. Caselle,⁶ J. Castillo Castellanos,³⁶ V. Catanescu,²¹ C. Cavicchioli,⁶ P. Cerello,¹⁴ B. Chang,³² S. Chapeland,⁶ J. L. Charvet,³⁶ S. Chattopadhyay,⁵⁷ S. Chattopadhyay,⁹ M. Cherney,⁶⁷ C. Cheshkov,⁶⁸ B. Cheynis,⁶⁸ E. Chiavassa,¹⁴ V. Chibante Barroso,⁶ D. D. Chinellato,⁶⁹ P. Chochula,⁶ M. Chojnacki,⁷⁰ P. Christakoglou,⁷⁰ C. H. Christensen,⁴⁴ P. Christiansen,⁷¹ T. Chujo,⁷² C. Cicalo,⁷³ L. Cifarelli,¹⁵ F. Cindolo,²⁶ J. Cleymans,⁶⁴ F. Coccetti,³⁵ J.-P. Coffin,⁴⁵ S. Coli,¹⁴ G. Conesa Balbastre,^{49,l} Z. Conesa del Valle,^{27,m} P. Constantin,⁶³ G. Contin,⁶⁰ J. G. Contreras,⁷⁴ T. M. Cormier,⁴⁶ Y. Corrales Morales,³⁴ I. Cortés Maldonado,⁷⁵ P. Cortese,⁷⁶ M. R. Cosentino,⁶⁹ F. Costa,⁶ M. E. Cotallo,⁵² E. Crescio,⁷⁴ P. Crochet,³⁷ E. Cuautle,⁷⁷ L. Cunqueiro,⁴⁹ G. D'Erasmus,¹⁸ A. Dainese,^{78,n} H. H. Dalsgaard,⁴⁴ A. Danu,⁷⁹ D. Das,⁵⁷ I. Das,⁵⁷ A. Dash,⁸⁰ S. Dash,¹⁴ S. De,⁹

- A. De Azevedo Moregula,⁴⁹ G. O. V. de Barros,⁸¹ A. De Caro,⁸² G. de Cataldo,⁸³ J. de Cuveland,¹⁷ A. De Falco,⁸⁴ D. De Gruttola,⁸² N. De Marco,¹⁴ S. De Pasquale,⁸² R. De Remigis,¹⁴ R. de Rooij,⁷⁰ H. Delagrange,²⁷ Y. Delgado Mercado,⁶⁶ G. Dellacasa,^{76,a} A. Deloff,⁸⁵ V. Demanov,⁶² E. Dénes,⁷ A. Deppman,⁸¹ D. Di Bari,¹⁸ C. Di Giglio,¹⁸ S. Di Liberto,⁸⁶ A. Di Mauro,⁶ P. Di Nezza,⁴⁹ T. Dietel,⁴² R. Divià,⁶ Ø. Djuvsland,¹ A. Dobrin,^{46,o} T. Dobrowolski,⁸⁵ I. Domínguez,⁷⁷ B. Dönigus,¹⁹ O. Dordic,⁵⁹ O. Driga,²⁷ A. K. Dubey,⁹ L. Ducroux,⁶⁸ P. Dupieux,³⁷ A. K. Dutta Majumdar,⁵⁷ M. R. Dutta Majumdar,⁹ D. Elia,⁸³ D. Emschermann,⁴² H. Engel,²² H. A. Erdal,⁸⁷ B. Espagnon,⁵⁸ M. Estienne,²⁷ S. Esumi,⁷² D. Evans,⁴⁰ S. Evrard,⁶ G. Eyyubova,⁵⁹ D. Fabris,⁸⁸ J. Faivre,²⁹ D. Falchieri,¹⁵ A. Fantoni,⁴⁹ M. Fasel,¹⁹ R. Fearick,⁶⁴ A. Fedunov,⁴³ D. Fehlker,¹ V. Fekete,⁶¹ D. Felea,⁷⁹ G. Feofilov,²⁰ A. Fernández Téllez,⁷⁵ A. Ferretti,³⁴ R. Ferretti,^{76,d} M. A. S. Figueredo,⁸¹ S. Filchagin,⁶² R. Fini,⁸³ D. Finogeev,⁸⁹ F. M. Fionda,¹⁸ E. M. Fiore,¹⁸ M. Floris,⁶ S. Foertsch,⁶⁴ P. Foka,¹⁹ S. Fokin,¹³ E. Fragiaco,⁹⁰ M. Fragiadakis,⁹¹ U. Frankenfeld,¹⁹ U. Fuchs,⁶ F. Furano,⁶ C. Furget,²⁹ M. Fusco Girard,⁸² J. J. Gaardhøje,⁴⁴ S. Gadrat,²⁹ M. Gagliardi,³⁴ A. Gago,⁶⁶ M. Gallio,³⁴ P. Ganoti,^{91,p} C. Garabatos,¹⁹ R. Gemme,⁷⁶ J. Gerhard,¹⁷ M. Germain,²⁷ C. Geuna,³⁶ A. Gheata,⁶ M. Gheata,⁶ B. Ghidini,¹⁸ P. Ghosh,⁹ M. R. Girard,⁹² G. Giraud,¹⁴ P. Giubellino,^{34,q} E. Gladysz-Dziadus,⁴¹ P. Glässel,⁶³ R. Gomez,⁹³ L. H. González-Trueba,⁸ P. González-Zamora,⁵² H. González Santos,⁷⁵ S. Gorbunov,¹⁷ S. Gotovac,⁹⁴ V. Grabski,⁸ L. K. Graczykowski,⁹² R. Gracjarek,⁶³ A. Grelli,⁷⁰ A. Grigoras,⁶ C. Grigoras,⁶ V. Grigoriev,⁵⁴ A. Grigoryan,⁹⁵ S. Grigoryan,⁴³ B. Grinyov,¹⁶ N. Grion,⁹⁰ P. Gros,⁷¹ J. F. Grosse-Oetringhaus,⁶ J.-Y. Grossiord,⁶⁸ R. Grosso,⁸⁸ F. Guber,⁸⁹ R. Guernane,²⁹ C. Guerra Gutierrez,⁶⁶ B. Guerzoni,¹⁵ K. Gulbrandsen,⁴⁴ H. Gulkanyan,⁹⁵ T. Gunji,⁹⁶ A. Gupta,⁴⁸ R. Gupta,⁴⁸ H. Gutbrod,¹⁹ Ø. Haaland,¹ C. Hadjidakis,⁵⁸ M. Haiduc,⁷⁹ H. Hamagaki,⁹⁶ G. Hamar,⁷ J. W. Harris,⁴ M. Hartig,²⁸ D. Hasch,⁴⁹ D. Hasegan,⁷⁹ D. Hatzifotiadou,²⁶ A. Hayrapetyan,^{95,d} M. Heide,⁴² M. Heinz,⁴ H. Helstrup,⁸⁷ A. Herghelegiu,²¹ C. Hernández,¹⁹ G. Herrera Corral,⁷⁴ N. Herrmann,⁶³ K. F. Hetland,⁸⁷ B. Hicks,⁴ P. T. Hille,⁴ B. Hippolyte,⁴⁵ T. Horaguchi,⁷² Y. Hori,⁹⁶ P. Hristov,⁶ I. Hřivnáčová,⁵⁸ M. Huang,¹ S. Huber,¹⁹ T. J. Humanic,²³ D. S. Hwang,⁹⁷ R. Ichou,²⁷ R. Ilkaev,⁶² I. Ilkiv,⁸⁵ M. Inaba,⁷² E. Incani,⁸⁴ G. M. Innocenti,³⁴ P. G. Innocenti,⁶ M. Ippolitov,¹³ M. Irfan,¹⁰ C. Ivan,¹⁹ A. Ivanov,²⁰ M. Ivanov,¹⁹ V. Ivanov,⁴⁷ A. Jachoňkowski,⁶ P. M. Jacobs,⁹⁸ L. Jancurová,⁴³ S. Jangal,⁴⁵ M. A. Janik,⁹² R. Janik,⁶¹ S. P. Jayarathna,^{53,r} S. Jena,⁹⁹ L. Jirden,⁶ G. T. Jones,⁴⁰ P. G. Jones,⁴⁰ P. Jovanović,⁴⁰ H. Jung,¹¹ W. Jung,¹¹ A. Jusko,⁴⁰ S. Kalcher,¹⁷ P. Kaliňák,³⁸ M. Kalisky,⁴² T. Kalliokoski,³² A. Kalweit,¹⁰⁰ R. Kamermans,^{70,a} K. Kanaki,¹ E. Kang,¹¹ J. H. Kang,¹⁰¹ V. Kaplin,⁵⁴ O. Karavichev,⁸⁹ T. Karavicheva,⁸⁹ E. Karpechev,⁸⁹ A. Kazantsev,¹³ U. Kebschull,²² R. Keidel,¹⁰² M. M. Khan,¹⁰ A. Khanzadeev,⁴⁷ Y. Kharlov,⁵⁵ B. Kileng,⁸⁷ D. J. Kim,³² D. S. Kim,¹¹ D. W. Kim,¹¹ H. N. Kim,¹¹ J. H. Kim,⁹⁷ J. S. Kim,¹¹ M. Kim,¹¹ M. Kim,¹⁰¹ S. Kim,⁹⁷ S. H. Kim,¹¹ S. Kirsch,^{6,s} I. Kisel,^{22,t} S. Kiselev,¹² A. Kisiel,⁶ J. L. Klay,¹⁰³ J. Klein,⁶³ C. Klein-Bösing,⁴² M. Kliemant,²⁸ A. Klovning,¹ A. Kluge,⁶ M. L. Knichel,¹⁹ K. Koch,⁶³ M. K. Köhler,¹⁹ R. Kolevatov,⁵⁹ A. Kolojvari,²⁰ V. Kondratiev,²⁰ N. Kondratyeva,⁵⁴ A. Konevskih,⁸⁹ E. Kornás,⁴¹ C. Kottachchi Kankanamge Don,⁴⁶ R. Kour,⁴⁰ M. Kowalski,⁴¹ S. Kox,²⁹ G. Koyithatta Meethalevedu,⁹⁹ K. Kozlov,¹³ J. Kral,³² I. Králik,³⁸ F. Kramer,²⁸ I. Kraus,^{100,u} T. Krawutschke,^{63,v} M. Kretz,¹⁷ M. Krivda,^{40,w} D. Krumborn,⁶³ M. Krus,⁵⁰ E. Kryshen,⁴⁷ M. Krzewicki,⁵¹ Y. Kucheriaev,¹³ C. Kuhn,⁴⁵ P. G. Kuijer,⁵¹ P. Kurashvili,⁸⁵ A. Kurepin,⁸⁹ A. B. Kurepin,⁸⁹ A. Kuryakin,⁶² S. Kuschpil,³ V. Kuschpil,³ M. J. Kweon,⁶³ Y. Kwon,¹⁰¹ P. La Rocca,³⁹ P. Ladrón de Guevara,^{52,x} V. Lafage,⁵⁸ C. Lara,²² D. T. Larsen,¹ C. Lazzeroni,⁴⁰ Y. Le Bornec,⁵⁸ R. Lea,⁶⁰ K. S. Lee,¹¹ S. C. Lee,¹¹ F. Lefèvre,²⁷ J. Lehnert,²⁸ L. Leistam,⁶ M. Lenhardt,²⁷ V. Lenti,⁸³ I. León Monzón,⁹³ H. León Vargas,²⁸ P. Lévai,⁷ X. Li,¹⁰⁴ R. Lietava,⁴⁰ S. Lindal,⁵⁹ V. Lindenstruth,^{22,t} C. Lippmann,^{6,u} M. A. Lisa,²³ L. Liu,¹ V. R. Loggins,⁴⁶ V. Loginov,⁵⁴ S. Lohn,⁶ D. Lohner,⁶³ C. Loizides,⁹⁸ X. Lopez,³⁷ M. López Noriega,⁵⁸ E. López Torres,² G. Løvnhøiden,⁵⁹ X.-G. Lu,⁶³ P. Luettig,²⁸ M. Lunardon,²⁵ G. Luparello,³⁴ L. Luquin,²⁷ C. Luzzi,⁶ K. Ma,⁶⁵ R. Ma,⁴ D. M. Madagodahettige-Don,⁵³ A. Maevskaya,⁸⁹ M. Mager,⁶ D. P. Mahapatra,⁸⁰ A. Maire,⁴⁵ M. Malaev,⁴⁷ I. Maldonado Cervantes,⁷⁷ L. Malinina,^{43,y} D. Mal'Kevich,¹² P. Malzacher,¹⁹ A. Mamonov,⁶² L. Manceau,³⁷ L. Mangotra,⁴⁸ V. Manko,¹³ F. Manso,³⁷ V. Manzari,⁸³ Y. Mao,^{65,z} J. Mareš,¹⁰⁵ G. V. Margagliotti,⁶⁰ A. Margotti,²⁶ A. Marín,¹⁹ I. Martashvili,¹⁰⁶ P. Martinengo,⁶ M. I. Martínez,⁷⁵ A. Martínez Davalos,⁸ G. Martínez García,²⁷ Y. Martynov,¹⁶ A. Mas,²⁷ S. Masciocchi,¹⁹ M. Maserà,³⁴ A. Masoni,⁷³ L. Massacrier,⁶⁸ M. Mastromarco,⁸³ A. Mastroserio,⁶ Z. L. Matthews,⁴⁰ A. Matyja,^{41,j} D. Mayani,⁷⁷ G. Mazza,¹⁴ M. A. Mazzoni,⁸⁶ F. Meddi,¹⁰⁷ A. Menchaca-Rocha,⁸ P. Mendez Lorenzo,⁶ J. Mercado Pérez,⁶³ P. Mereu,¹⁴ Y. Miake,⁷² J. Midori,¹⁰⁸ L. Milano,³⁴ J. Milosevic,^{59,aa} A. Mischke,⁷⁰ D. Miśkowiec,^{19,q} C. Mitu,⁷⁹ J. Mlynarz,⁴⁶ B. Mohanty,⁹ L. Molnar,⁶ L. Montaña Zetina,⁷⁴ M. Monteno,¹⁴ E. Montes,⁵² M. Morando,²⁵ D. A. Moreira De Godoy,⁸¹ S. Moretto,²⁵ A. Morsch,⁶ V. Muccifora,⁴⁹ E. Mudnic,⁹⁴ H. Müller,⁶ S. Muhuri,⁹ M. G. Munhoz,⁸¹ J. Munoz,⁷⁵ L. Musa,⁶

A. Musso,¹⁴ B. K. Nandi,⁹⁹ R. Nania,²⁶ E. Nappi,⁸³ C. Nattrass,¹⁰⁶ F. Navach,¹⁸ S. Navin,⁴⁰ T. K. Nayak,⁹ S. Nazarenko,⁶² G. Nazarov,⁶² A. Nedosekin,¹² F. Nendaz,⁶⁸ J. Newby,¹⁰⁹ M. Nicassio,¹⁸ B. S. Nielsen,⁴⁴ S. Nikolaev,¹³ V. Nikolic,²⁴ S. Nikulin,¹³ V. Nikulin,⁴⁷ B. S. Nilsen,⁶⁷ M. S. Nilsson,⁵⁹ F. Noferini,²⁶ G. Nooren,⁷⁰ N. Novitzky,³² A. Nyanin,¹³ A. Nyatha,⁹⁹ C. Nygaard,⁴⁴ J. Nystrand,¹ H. Obayashi,¹⁰⁸ A. Ochirov,²⁰ H. Oeschler,¹⁰⁰ S. K. Oh,¹¹ J. Oliencz,⁹² C. Oppedisano,¹⁴ A. Ortiz Velasquez,⁷⁷ G. Ortona,^{6,h} A. Oskarsson,⁷¹ P. Ostrowski,⁹² I. Otterlund,⁷¹ J. Otwinowski,¹⁹ G. Øvrebekk,¹ K. Oyama,⁶³ K. Ozawa,⁹⁶ Y. Pachmayer,⁶³ M. Pacher,⁵⁰ F. Padilla,³⁴ P. Pagano,^{6,bb} G. Pačić,⁷⁷ F. Painke,¹⁷ C. Pajares,³⁰ S. Pal,³⁶ S. K. Pal,⁹ A. Palaha,⁴⁰ A. Palmeri,³³ G. S. Pappalardo,³³ W. J. Park,¹⁹ V. Paticchio,⁸³ A. Pavlinov,⁴⁶ T. Pawlak,⁹² T. Peitzmann,⁷⁰ D. Peresunko,¹³ C. E. Pérez Lara,⁵¹ D. Perini,⁶ D. Perrino,¹⁸ W. Peryt,⁹² A. Pesci,²⁶ V. Peskov,^{6,cc} Y. Pestov,¹¹⁰ A. J. Peters,⁶ V. Petráček,⁵⁰ M. Petris,²¹ P. Petrov,⁴⁰ M. Petrovici,²¹ C. Petta,³⁹ S. Piano,⁹⁰ A. Piccotti,¹⁴ M. Pikna,⁶¹ P. Pillot,²⁷ O. Pinazza,⁶ L. Pinsky,⁵³ N. Pitz,²⁸ F. Piuz,⁶ D. B. Piyarathna,^{46,dd} R. Platt,⁴⁰ M. Płoskoń,⁹⁸ J. Pluta,⁹² T. Pocheptsov,^{43,ee} S. Pochybova,⁷ P. L. M. Podesta-Lerma,⁹³ M. G. Poghosyan,³⁴ K. Polák,¹⁰⁵ B. Polichtchouk,⁵⁵ A. Pop,²¹ V. Pospíšil,⁵⁰ B. Potukuchi,⁴⁸ S. K. Prasad,^{46,ff} R. Preghenella,³⁵ F. Prino,¹⁴ C. A. Pruneau,⁴⁶ I. Pshenichnov,⁸⁹ G. Puddu,⁸⁴ A. Pulvirenti,^{39,d} V. Punin,⁶² M. Putiš,⁵⁶ J. Putschke,⁴ E. Quercigh,⁶ H. Qvigstad,⁵⁹ A. Rachevski,⁹⁰ A. Rademakers,⁶ O. Rademakers,⁶ S. Radomski,⁶³ T. S. Rähä,³² J. Rak,³² A. Rakotozafindrabe,³⁶ L. Ramello,⁷⁶ A. Ramírez Reyes,⁷⁴ M. Rammner,⁴² R. Raniwala,¹¹¹ S. Raniwala,¹¹¹ S. S. Räsänen,³² K. F. Read,¹⁰⁶ J. S. Real,²⁹ K. Redlich,⁸⁵ R. Renfordt,²⁸ A. R. Reolon,⁴⁹ A. Reshetin,⁸⁹ F. Rettig,¹⁷ J.-P. Revol,⁶ K. Reygers,⁶³ H. Ricaud,¹⁰⁰ L. Riccati,¹⁴ R. A. Ricci,⁷⁸ M. Richter,^{1,gg} P. Riedler,⁶ W. Riegler,⁶ F. Riggi,³⁹ A. Rivetti,¹⁴ M. Rodríguez Cahuantzi,⁷⁵ D. Rohr,¹⁷ D. Röhrich,¹ R. Romita,¹⁹ F. Ronchetti,⁴⁹ P. Rosinský,⁶ P. Rosnet,³⁷ S. Rossegger,⁶ A. Rossi,²⁵ F. Roukoutakis,⁹¹ S. Rousseau,⁵⁸ C. Roy,^{27,m} P. Roy,⁵⁷ A. J. Rubio Montero,⁵² R. Rui,⁶⁰ I. Rusanov,⁶ E. Ryabinkin,¹³ A. Rybicki,⁴¹ S. Sadovsky,⁵⁵ K. Šafařík,⁶ R. Sahoo,²⁵ P. K. Sahu,⁸⁰ P. Saiz,⁶ S. Sakai,⁹⁸ D. Sakata,⁷² C. A. Salgado,³⁰ T. Samanta,⁹ S. Sambyal,⁴⁸ V. Samsonov,⁴⁷ L. Šándor,³⁸ A. Sandoval,⁸ M. Sano,⁷² S. Sano,⁹⁶ R. Santo,⁴² R. Santoro,⁸³ J. Sarkamo,³² P. Saturnini,³⁷ E. Scapparone,²⁶ F. Scarlassara,²⁵ R. P. Scharenberg,¹¹² C. Schiaua,²¹ R. Schicker,⁶³ C. Schmidt,¹⁹ H. R. Schmidt,¹⁹ S. Schreiner,⁶ S. Schuchmann,²⁸ J. Schukraft,⁶ Y. Schutz,^{27,d} K. Schwarz,¹⁹ K. Schweda,⁶³ G. Scioli,¹⁵ E. Scomparin,¹⁴ P. A. Scott,⁴⁰ R. Scott,¹⁰⁶ G. Segato,²⁵ S. Senyukov,⁷⁶ J. Seo,¹¹ S. Serici,⁸⁴ E. Serradilla,⁵² A. Sevcenco,⁷⁹ G. Shabratova,⁴³ R. Shahoyan,⁶ N. Sharma,⁵ S. Sharma,⁴⁸ K. Shigaki,¹⁰⁸ M. Shimomura,⁷² K. Shtejer,² Y. Sibiriak,¹³ M. Siciliano,³⁴ E. Sicking,⁶ T. Siemiarzucuk,⁸⁵ A. Silenzi,¹⁵ D. Silvermyr,³¹ G. Simonetti,^{6,hh} R. Singaraju,⁹ R. Singh,⁴⁸ B. C. Sinha,⁹ T. Sinha,⁵⁷ B. Sitar,⁶¹ M. Sitta,⁷⁶ T. B. Skaali,⁵⁹ K. Skjerdal,¹ R. Smakal,⁵⁰ N. Smirnov,⁴ R. Snellings,^{51,ii} C. Søgaard,⁴⁴ A. Soloviev,⁵⁵ R. Soltz,¹⁰⁹ H. Son,⁹⁷ M. Song,¹⁰¹ C. Soos,⁶ F. Soramel,²⁵ M. Spyropoulou-Stassinaki,⁹¹ B. K. Srivastava,¹¹² J. Stachel,⁶³ I. Stan,⁷⁹ G. Stefanek,⁸⁵ G. Stefanini,⁶ T. Steinbeck,^{22,i} E. Stenlund,⁷¹ G. Steyn,⁶⁴ D. Stocco,²⁷ R. Stock,²⁸ M. Stolpovskiy,⁵⁵ P. Strmen,⁶¹ A. A. P. Suaide,⁸¹ M. A. Subieta Vásquez,³⁴ T. Sugitate,¹⁰⁸ C. Suire,⁵⁸ M. Šumbera,³ T. Susa,²⁴ D. Swoboda,⁶ T. J. M. Symons,⁹⁸ A. Szanto de Toledo,⁸¹ I. Szarka,⁶¹ A. Szostak,¹ C. Tagridis,⁹¹ J. Takahashi,⁶⁹ J. D. Tapia Takaki,⁵⁸ A. Tauro,⁶ M. Tavlet,⁶ G. Tejeda Muñoz,⁷⁵ A. Telesca,⁶ C. Terrevoli,¹⁸ J. Thäder,¹⁹ D. Thomas,⁷⁰ J. H. Thomas,¹⁹ R. Tieulent,⁶⁸ A. R. Timmins,^{46,g} D. Tlusty,⁵⁰ A. Toia,⁶ H. Torii,¹⁰⁸ L. Toscano,⁶ F. Tosello,¹⁴ T. Traczyk,⁹² D. Truesdale,²³ W. H. Trzaska,³² A. Tumkin,⁶² R. Turrisi,⁸⁸ A. J. Turvey,⁶⁷ T. S. Tveter,⁵⁹ J. Ulery,²⁸ K. Ullaland,¹ A. Uras,⁸⁴ J. Urbán,⁵⁶ G. M. Urciuoli,⁸⁶ G. L. Usai,⁸⁴ A. Vacchi,⁹⁰ M. Vala,^{43,w} L. Valencia Palomo,⁵⁸ S. Vallero,⁶³ N. van der Kolk,⁵¹ M. van Leeuwen,⁷⁰ P. Vande Vyvre,⁶ L. Vannucci,⁷⁸ A. Vargas,⁷⁵ R. Varma,⁹⁹ M. Vasileiou,⁹¹ A. Vasiliev,¹³ V. Vechernin,²⁰ M. Venaruzzo,⁶⁰ E. Vercellin,³⁴ S. Vergara,⁷⁵ R. Vernet,¹¹³ M. Verweij,⁷⁰ L. Vickovic,⁹⁴ G. Viesti,²⁵ O. Vikhlyantsev,⁶² Z. Vilakazi,⁶⁴ O. Villalobos Baillie,⁴⁰ A. Vinogradov,¹³ L. Vinogradov,²⁰ Y. Vinogradov,⁶² T. Virgili,⁸² Y. P. Viyogi,⁹ A. Vodopyanov,⁴³ K. Voloshin,¹² S. Voloshin,⁴⁶ G. Volpe,¹⁸ B. von Haller,⁶ D. Vranic,¹⁹ J. Vrláková,⁵⁶ B. Vulpescu,³⁷ B. Wagner,¹ V. Wagner,⁵⁰ R. Wan,^{45,ij} D. Wang,⁶⁵ Y. Wang,⁶³ Y. Wang,⁶⁵ K. Watanabe,⁷² J. P. Wessels,⁴² U. Westerhoff,⁴² J. Wiechula,⁶³ J. Wikne,⁵⁹ M. Wilde,⁴² A. Wilk,⁴² G. Wilk,⁸⁵ M. C. S. Williams,²⁶ B. Windelband,⁶³ H. Yang,³⁶ S. Yasnopolskiy,¹³ J. Yi,¹¹⁴ Z. Yin,⁶⁵ H. Yokoyama,⁷² I.-K. Yoo,¹¹⁴ X. Yuan,⁶⁵ I. Yushmanov,¹³ E. Zabrodin,⁵⁹ C. Zampolli,⁶ S. Zaporozhets,⁴³ A. Zarochentsev,²⁰ P. Závada,¹⁰⁵ H. Zbroszczyk,⁹² P. Zelnicek,²² A. Zenin,⁵⁵ I. Zgura,⁷⁹ M. Zhalov,⁴⁷ X. Zhang,^{65,b} D. Zhou,⁶⁵ X. Zhu,⁶⁵ A. Zichichi,^{15,kk} G. Zinovyev,¹⁶ Y. Zoccarato,⁶⁸ and M. Zynovyev¹⁶

(ALICE Collaboration)

- ¹*Department of Physics and Technology, University of Bergen, Bergen, Norway*
- ²*Centro de Aplicaciones Tecnológicas y Desarrollo Nuclear (CEADEN), Havana, Cuba*
- ³*Nuclear Physics Institute, Academy of Sciences of the Czech Republic, Řež u Prahy, Czech Republic*
- ⁴*Yale University, New Haven, Connecticut, USA*
- ⁵*Physics Department, Panjab University, Chandigarh, India*
- ⁶*European Organization for Nuclear Research (CERN), Geneva, Switzerland*
- ⁷*KFKI Research Institute for Particle and Nuclear Physics, Hungarian Academy of Sciences, Budapest, Hungary*
- ⁸*Instituto de Física, Universidad Nacional Autónoma de México, Mexico City, Mexico*
- ⁹*Variable Energy Cyclotron Centre, Kolkata, India*
- ¹⁰*Department of Physics, Aligarh Muslim University, Aligarh, India*
- ¹¹*Gangneung-Wonju National University, Gangneung, South Korea*
- ¹²*Institute for Theoretical and Experimental Physics, Moscow, Russia*
- ¹³*Russian Research Centre Kurchatov Institute, Moscow, Russia*
- ¹⁴*Sezione INFN, Turin, Italy*
- ¹⁵*Dipartimento di Fisica, dell'Università and Sezione INFN, Bologna, Italy*
- ¹⁶*Bogolyubov Institute for Theoretical Physics, Kiev, Ukraine*
- ¹⁷*Frankfurt Institute for Advanced Studies, Johann Wolfgang Goethe-Universität Frankfurt, Frankfurt, Germany*
- ¹⁸*Dipartimento Interateneo di Fisica, "M. Merlin" and Sezione INFN, Bari, Italy*
- ¹⁹*Research Division and ExtreMe Matter Institute EMMI, GSI Helmholtzzentrum für Schwerionenforschung, Darmstadt, Germany*
- ²⁰*V. Fock Institute for Physics, St. Petersburg State University, St. Petersburg, Russia*
- ²¹*National Institute for Physics and Nuclear Engineering, Bucharest, Romania*
- ²²*Kirchhoff-Institut für Physik, Ruprecht-Karls-Universität Heidelberg, Heidelberg, Germany*
- ²³*Department of Physics, Ohio State University, Columbus, Ohio, USA*
- ²⁴*Rudjer Bošković Institute, Zagreb, Croatia*
- ²⁵*Dipartimento di Fisica, dell'Università and Sezione INFN, Padova, Italy*
- ²⁶*Sezione INFN, Bologna, Italy*
- ²⁷*SUBATECH, Ecole des Mines de Nantes, Université de Nantes, CNRS-IN2P3, Nantes, France*
- ²⁸*Institut für Kernphysik, Johann Wolfgang Goethe-Universität Frankfurt, Frankfurt, Germany*
- ²⁹*Laboratoire de Physique Subatomique et de Cosmologie (LPSC), USA Université Joseph Fourier, CNRS-IN2P3, Institut Polytechnique de Grenoble, Grenoble, France*
- ³⁰*Departamento de Física de Partículas and IGFAE, Universidad de Santiago de Compostela, Santiago de Compostela, Spain*
- ³¹*Oak Ridge National Laboratory, Oak Ridge, Tennessee, USA*
- ³²*Helsinki Institute of Physics (HIP) and University of Jyväskylä, Jyväskylä, Finland*
- ³³*Sezione INFN, Catania, Italy*
- ³⁴*Dipartimento di Fisica, Sperimentale dell'Università and Sezione INFN, Turin, Italy*
- ³⁵*Centro Fermi-Centro Studi e Ricerche e Museo Storico della Fisica "Enrico Fermi", Rome, Italy*
- ³⁶*Commissariat à l'Énergie Atomique, IRFU, Saclay, France*
- ³⁷*Laboratoire de Physique Corpusculaire (LPC), Clermont Université, Université Blaise Pascal, CNRS-IN2P3, Clermont-Ferrand, France*
- ³⁸*Institute of Experimental Physics, Slovak Academy of Sciences, Košice, Slovakia*
- ³⁹*Dipartimento di Fisica e Astronomia, dell'Università and Sezione INFN, Catania, Italy*
- ⁴⁰*School of Physics and Astronomy, University of Birmingham, Birmingham, United Kingdom*
- ⁴¹*The Henryk Niewodniczanski Institute of Nuclear Physics, Polish Academy of Sciences, Cracow, Poland*
- ⁴²*Institut für Kernphysik, Westfälische Wilhelms-Universität Münster, Münster, Germany*
- ⁴³*Joint Institute for Nuclear Research (JINR), Dubna, Russia*
- ⁴⁴*Niels Bohr Institute, University of Copenhagen, Copenhagen, Denmark*
- ⁴⁵*Institut Pluridisciplinaire Hubert Curien (IPHC), Université de Strasbourg, CNRS-IN2P3, Strasbourg, France*
- ⁴⁶*Wayne State University, Detroit, Michigan, USA*
- ⁴⁷*Petersburg Nuclear Physics Institute, Gatchina, Russia*
- ⁴⁸*Physics Department, University of Jammu, Jammu, India*
- ⁴⁹*Laboratori Nazionali di Frascati, INFN, Frascati, Italy*
- ⁵⁰*Faculty of Nuclear Sciences and Physical Engineering, Czech Technical University in Prague, Prague, Czech Republic*
- ⁵¹*Nikhef, National Institute for Subatomic Physics, Amsterdam, Netherlands*
- ⁵²*Centro de Investigaciones Energéticas Medioambientales y Tecnológicas (CIEMAT), Madrid, Spain*
- ⁵³*University of Houston, Houston, Texas, USA*
- ⁵⁴*Moscow Engineering Physics Institute, Moscow, Russia*
- ⁵⁵*Institute for High Energy Physics, Protvino, Russia*
- ⁵⁶*Faculty of Science, P.J. Šafárik University, Košice, Slovakia*
- ⁵⁷*Saha Institute of Nuclear Physics, Kolkata, India*
- ⁵⁸*Institut de Physique Nucléaire d'Orsay (IPNO), Université Paris-Sud, CNRS-IN2P3, Orsay, France*
- ⁵⁹*Department of Physics, University of Oslo, Oslo, Norway*

- ⁶⁰*Dipartimento di Fisica, dell'Università and Sezione INFN, Trieste, Italy*
- ⁶¹*Faculty of Mathematics, Physics and Informatics, Comenius University, Bratislava, Slovakia*
- ⁶²*Russian Federal Nuclear Center (VNIIEF), Sarov, Russia*
- ⁶³*Physikalisches Institut, Ruprecht-Karls-Universität Heidelberg, Heidelberg, Germany*
- ⁶⁴*Physics Department, University of Cape Town, iThemba LABS, Cape Town, South Africa*
- ⁶⁵*Hua-Zhong Normal University, Wuhan, China*
- ⁶⁶*Sección Física, Departamento de Ciencias, Pontificia Universidad Católica del Perú, Lima, Peru*
- ⁶⁷*Physics Department, Creighton University, Omaha, Nebraska, USA*
- ⁶⁸*Université de Lyon, Université Lyon 1, CNRS/IN2P3, IPN-Lyon, Villeurbanne, France*
- ⁶⁹*Universidade Estadual de Campinas (UNICAMP), Campinas, Brazil*
- ⁷⁰*Nikhef, National Institute for Subatomic Physics and Institute for Subatomic Physics of Utrecht University, Utrecht, Netherlands*
- ⁷¹*Division of Experimental High Energy Physics, University of Lund, Lund, Sweden*
- ⁷²*University of Tsukuba, Tsukuba, Japan*
- ⁷³*Sezione INFN, Cagliari, Italy*
- ⁷⁴*Centro de Investigación y de Estudios Avanzados (CINVESTAV), Mexico City and Mérida, Mexico*
- ⁷⁵*Benemérita Universidad Autónoma de Puebla, Puebla, Mexico*
- ⁷⁶*Dipartimento di Scienze e Tecnologie, Avanzate dell'Università del Piemonte Orientale and Gruppo Collegato INFN, Alessandria, Italy*
- ⁷⁷*Instituto de Ciencias Nucleares, Universidad Nacional Autónoma de México, Mexico City, Mexico*
- ⁷⁸*Laboratori Nazionali di Legnaro, INFN, Legnaro, Italy*
- ⁷⁹*Institute of Space Sciences (ISS), Bucharest, Romania*
- ⁸⁰*Institute of Physics, Bhubaneswar, India*
- ⁸¹*Universidade de São Paulo (USP), São Paulo, Brazil*
- ⁸²*Dipartimento di Fisica, 'E.R. Caianiello' dell'Università and Gruppo Collegato INFN, Salerno, Italy*
- ⁸³*Sezione INFN, Bari, Italy*
- ⁸⁴*Dipartimento di Fisica, dell'Università and Sezione INFN, Cagliari, Italy*
- ⁸⁵*Soltan Institute for Nuclear Studies, Warsaw, Poland*
- ⁸⁶*Sezione INFN, Rome, Italy*
- ⁸⁷*Faculty of Engineering, Bergen University College, Bergen, Norway*
- ⁸⁸*Sezione INFN, Padova, Italy*
- ⁸⁹*Institute for Nuclear Research, Academy of Sciences, Moscow, Russia*
- ⁹⁰*Sezione INFN, Trieste, Italy*
- ⁹¹*Physics Department, University of Athens, Athens, Greece*
- ⁹²*Warsaw University of Technology, Warsaw, Poland*
- ⁹³*Universidad Autónoma de Sinaloa, Culiacán, Mexico*
- ⁹⁴*Technical University of Split FESB, Split, Croatia*
- ⁹⁵*Yerevan Physics Institute, Yerevan, Armenia*
- ⁹⁶*University of Tokyo, Tokyo, Japan*
- ⁹⁷*Department of Physics, Sejong University, Seoul, South Korea*
- ⁹⁸*Lawrence Berkeley National Laboratory, Berkeley, California, USA*
- ⁹⁹*Indian Institute of Technology, Mumbai, India*
- ¹⁰⁰*Institut für Kernphysik, Technische Universität Darmstadt, Darmstadt, Germany*
- ¹⁰¹*Yonsei University, Seoul, South Korea*
- ¹⁰²*Zentrum für Technologietransfer und Telekommunikation (ZTT), Fachhochschule Worms, Worms, Germany*
- ¹⁰³*California Polytechnic State University, San Luis Obispo, California, USA*
- ¹⁰⁴*China Institute of Atomic Energy, Beijing, China*
- ¹⁰⁵*Institute of Physics, Academy of Sciences of the Czech Republic, Prague, Czech Republic*
- ¹⁰⁶*University of Tennessee, Knoxville, Tennessee, USA*
- ¹⁰⁷*Dipartimento di Fisica, dell'Università "La Sapienza" and Sezione INFN, Rome, Italy*
- ¹⁰⁸*Hiroshima University, Hiroshima, Japan*
- ¹⁰⁹*Lawrence Livermore National Laboratory, Livermore, California, USA*
- ¹¹⁰*Budker Institute for Nuclear Physics, Novosibirsk, Russia*
- ¹¹¹*Physics Department, University of Rajasthan, Jaipur, India*
- ¹¹²*Purdue University, West Lafayette, Indiana, USA*
- ¹¹³*Centre de Calcul de l'IN2P3, Villeurbanne, France*
- ¹¹⁴*Pusan National University, Pusan, South Korea*

^aDeceased.^bAlso at Laboratoire de Physique Corpusculaire (LPC), Clermont Université, Université Blaise Pascal, CNRS-IN2P3, Clermont-Ferrand, France.

- ^cNow at Centro Fermi-Centro Studi e Ricerche e Museo Storico della Fisica “Enrico Fermi”, Rome, Italy; Now at European Organization for Nuclear Research (CERN), Geneva, Switzerland.
- ^dAlso at European Organization for Nuclear Research (CERN), Geneva, Switzerland.
- ^eNow at Physikalisches Institut, Ruprecht-Karls-Universität Heidelberg, Heidelberg, Germany; Now at Frankfurt Institute for Advanced Studies, Johann Wolfgang Goethe-Universität Frankfurt, Frankfurt, Germany.
- ^fNow at Sezione INFN, Turin, Italy.
- ^gNow at University of Houston, Houston, TX, USA.
- ^hAlso at Dipartimento di Fisica Sperimentale dell’Università and Sezione INFN, Turin, Italy.
- ⁱAlso at Dipartimento di Fisica, dell’Università, Udine, Italy.
- ^jNow at SUBATECH, Ecole des Mines de Nantes, Université de Nantes, CNRS-IN2P3, Nantes, France.
- ^kNow at Centro de Investigación y de Estudios Avanzados (CINVESTAV), Mexico City and Mérida, Mexico; Now at Benemérita Universidad Autónoma de Puebla, Puebla, Mexico.
- ^lNow at Laboratoire de Physique Subatomique et de Cosmologie (LPSC), Université Joseph Fourier, CNRS-IN2P3, Institut Polytechnique de Grenoble, Grenoble, France.
- ^mNow at Institut Pluridisciplinaire Hubert Curien (IPHC), Université de Strasbourg, CNRS-IN2P3, Strasbourg, France.
- ⁿNow at Sezione INFN, Padova, Italy.
- ^oAlso at Division of Experimental High Energy Physics, University of Lund, Lund, Sweden.
- ^pNow at Oak Ridge National Laboratory, Oak Ridge, TN, USA.
- ^qNow at European Organization for Nuclear Research (CERN), Geneva, Switzerland.
- ^rAlso at Wayne State University, Detroit, MI, USA.
- ^sAlso at Frankfurt Institute for Advanced Studies, Johann Wolfgang Goethe-Universität Frankfurt, Frankfurt, Germany.
- ^tNow at Frankfurt Institute for Advanced Studies, Johann Wolfgang Goethe-Universität Frankfurt, Frankfurt, Germany.
- ^uNow at Research Division and ExtreMe Matter Institute EMMI, GSI Helmholtzzentrum für Schwerionenforschung, Darmstadt, Germany.
- ^vAlso at Fachhochschule Köln, Köln, Germany.
- ^wAlso at Institute of Experimental Physics, Slovak Academy of Sciences, Košice, Slovakia.
- ^xNow at Instituto de Ciencias Nucleares, Universidad Nacional Autónoma de México, Mexico City, Mexico.
- ^yAlso at M. V. Lomonosov Moscow State University, D. V. Skobeltsyn Institute of Nuclear Physics, Moscow, Russia.
- ^zAlso at Laboratoire de Physique Subatomique et de Cosmologie (LPSC), Université Joseph Fourier, CNRS-IN2P3, Institut Polytechnique de Grenoble, Grenoble, France.
- ^{aa}Also at “Vinča” Institute of Nuclear Sciences, Belgrade, Serbia.
- ^{bb}Also at Dipartimento di Fisica ‘E. R. Caianiello’ dell’Università and Gruppo Collegato INFN, Salerno, Italy.
- ^{cc}Also at Instituto de Ciencias Nucleares, Universidad Nacional Autónoma de México, Mexico City, Mexico.
- ^{dd}Also at University of Houston, Houston, TX, USA.
- ^{ee}Also at Department of Physics, University of Oslo, Oslo, Norway.
- ^{ff}Also at Variable Energy Cyclotron center, Kolkata, India.
- ^{gg}Now at Department of Physics, University of Oslo, Oslo, Norway.
- ^{hh}Also at Dipartimento Interateneo di Fisica ‘M. Merlin’ and Sezione INFN, Bari, Italy.
- ⁱⁱNow at Nikhef, National Institute for Subatomic Physics and Institute for Subatomic Physics of Utrecht University, Utrecht, Netherlands.
- ^{jj}Also at Hua-Zhong Normal University, Wuhan, China.
- ^{kk}Also at Centro Fermi-Centro Studi e Ricerche e Museo Storico della Fisica “Enrico Fermi,” Rome, Italy.